

GPO PRICE \$ _____

CFSTI PRICE(S) \$ _____

Hard copy (HC) 2.50

Microfiche (MF) 175

ff 653 July 65

FACILITY FORM 60
N66 32681
(ACCESSION NUMBER)
87
(PAGES)
CR-76912
(NASA CR OR TMX OR AD NUMBER)

(THRU)
/ (CODE)
01 (CATEGORY)

DECEMBER 1965

2-80-65-1

TECHNICAL SUMMARY REPORT

DYNAMICS OF SEPARATED FLOW OVER BLUNT BODIES

PREPARED BY: Lars Eric Ericsson
Lars Eric Ericsson • Staff Engineer Senior • Flight Technology

PREPARED BY: J. Peter Reding
J. Peter Reding • Dynamics Engineer Senior • Aero-Hydrodynamics

APPROVED BY: M. Tucker
M. Tucker • Manager • Flight Technology

Prepared under Contract NAS 8-5338
For
Aerodynamics Division, Aero-Astrodynamic Laboratory,
George C. Marshall Space Flight Center,
National Aeronautics and Space Administration,
Huntsville, Alabama

Lockheed

MISSILES & SPACE COMPANY

A GROUP DIVISION OF LOCKHEED AIRCRAFT CORPORATION

SUNNYVALE, CALIFORNIA

ABSTRACT

The results of a study of the dynamics of separated flow over blunt bodies are reported. The various types of flow separation occurring on the Saturn-Apollo launch vehicles have been examined and analyzed in detail. The analytical relationships between unsteady and static characteristics are derived for different separated flow patterns using quasi-steady methods. The detailed results are reported in special interim reports. This summary report is intended to present in condensed form the progress and final results of the study. It is shown that separated flow can produce large and highly nonlinear aerodynamic loads which have a dominant influence on the vehicle dynamics, be it a rocket booster or a reentry vehicle. In all cases where experimental dynamic data have been available, the quasi-steady predictions show good agreement with the experimental results.

CONTENTS

Section		Page
	ABSTRACT	iii
	ILLUSTRATIONS	vi
1	SUMMARY	1-1
2	INTRODUCTION	2-1
3	STATEMENT OF PROBLEM	3-1
4	QUASI-STEADY ANALYSIS	4-1
5	DISCUSSION OF RESULTS	5-1
6	CONCLUSIONS	6-1
7	REFERENCES	7-1
8	RECOMMENDATIONS FOR FUTURE STUDY	8-1
Appendix		
A	NOMENCLATURE	A-1
B	REPORTS THAT HAVE SUPPLIED SUBSTANTIAL DATA INPUTS TO THE STUDY OF DYNAMICS OF SEPARATED FLOW OVER BLUNT BODIES	B-1
C	GENERALIZED QUASI-STEADY METHODS	C-1

ILLUSTRATIONS

Figure		Page
2-1	Supersonic Flow Field on the Saturn-Apollo Launch Vehicle	2-2
2-2	Supersonic Static and Dyanmic Loads on the Saturn Booster, ($\alpha = 0$)	2-3
2-3	Subsonic Static and Dyanmic Loads on the Saturn Booster, Tower Off ($\alpha = 0$)	2-4
4-1	Coordinate System and Definitions	4-2
4-2	Dynamic Time Lag Effects	4-5
4-3	Wake-Induced Dynamic Effects for Various Oscillation Centers	4-7
5-1	Effect of Escape Rocket on Apollo Command Module Forces at $M = 1.0$	5-2
5-2	Comparison of Angle of Attack and Spike Deflection Effects	5-3
5-3	Optimum Spike Length and the Associated Minimum Forebody Drag on a Hemisphere-Nose Body at Supersonic and Hypersonic Mach Numbers	5-4
5-4	Relative Loss in Drag Reduction for Non-Optimum Spike Length	5-5
5-5	Static Stability Effects of a Flow Separation Disk at Supersonic Mach Numbers	5-7
5-6	Separated Flow Pattern and Pitch Damping of a Cylindrical Body With a Flow Separation Disk	5-8
5-7	Local Crossflow Effect on the Submerged Body (Directing Wake Source)	5-10
5-8	Correlation Between Wake Source Base Pressure Sensitivity and Submerged Body Local Loads. (Non-Directing Wake Source)	5-11
5-9	Wake Translation Effects on the Submerged Body (Directing and Non-Directing Wake Sources)	5-13
5-10	Comparison of Wake Source Directing Effects	5-14
5-11	Induced Forces on the Apollo Command Module by the Wake From the Disk-Off Escape Rocket	5-15
5-12	Saturn Forebody Pressure Distribution With Escape System Removed at $M = 0.9$	5-16

Figure		Page
5-13	Effect of Nose-Induced Separation on Pressure and Load Distribution Over a Blunt-Nosed Cylinder-Flare Body	5-17
5-14	Comparison Between Quasi-Steady Predictions and Measured Pitch Damping of a Blunt-Nosed Cylinder-Flare Body at Transonic Mach Numbers	5-19
5-15	Nonlinear Amplitude Effects Caused by Nose-Induced Separation	5-20
5-16	Dynamic Effects of Separation-Induced Pitch Moment Discontinuity at Transonic Mach Numbers	5-21
5-17	Large Amplitude Pitch Damping	5-23
5-18	Comparison Between Subsonic and Supersonic Separated Flow Patterns	5-24
5-19	Shock-Induced Separation Effects on the Saturn Forebody Pressure Distribution	5-25
5-20	Boundary Layer Thickness Effect on Shock-Induced Separation	5-26
5-21	Pressures and Loads on the Apollo Command Module Shoulder	5-28
5-22	Critical Cylinder Length Effects on the Saturn Forebody	5-29
5-23	Aerodynamic Damping at $\alpha = 0$ of the Saturn I-Apollo Launch Vehicle With Escape Rocket, Disk-On	5-31
5-24	Aerodynamic Damping at $\alpha = 0$ of the Saturn I-Apollo Launch Vehicle With Escape Rocket, Disk-Off	5-32
5-25	Aerodynamic Damping at $\alpha = 0$ of the Saturn I-Apollo Vehicle Without Escape Rocket	5-33
5-26	Forebody Damping at $\alpha = 0$ for the Second Bending Mode of the Saturn-Apollo Launch Vehicle With Escape Rocket, Disk-On and Disk-Off	5-34
5-27	Forebody Damping at $\alpha = 0$ for the Second Bending Mode of the Saturn-Apollo Launch Vehicle Without Escape Rocket	5-35
5-28	Effect of Flare Geometry on Rigid Body Damping	5-36

Section 1
SUMMARY

32681

Certain geometric features common to many manned boosters, such as tower-mounted escape rockets and steep interstage flares, are sources of flow separation that may dominate the vehicle dynamics in the transonic Mach number range where the dynamic pressure is large. Such is the case with the Saturn-Apollo manned boosters. Several specific types of flow separation occurring on the Saturn-Apollo launch vehicles have been singled out for special study. The dynamic effects of separated flow were derived using experimental static loads and quasi-steady methods. These various separate efforts are reported in detail in special interim reports, and only the highlights and main conclusive results are included in the present technical summary report. The quasi-steady predictions are shown to agree well with experimental dynamic results. Thus is the transonic dynamic instability of blunt-nosed, cylinder-flare reentry bodies closely predicted, and the undamping effect of a flow separation disk is readily forecasted. Furthermore, the aerodynamic damping measured on elastic models of the Saturn I-Apollo launch vehicle agreed well with the quasi-steady predictions, making it possible to predict with satisfactory accuracy the full-scale aeroelastic characteristics of the Saturn I booster, including several last minute changes in vehicle geometry, structure, and trajectory.

Section 2

INTRODUCTION

Since any rocket design is a compromise between a number of conflicting requirements for various flight regimes, it is not surprising that many recent designs are not aerodynamically clean. As a result, many vehicles – both ascent and entry vehicles – exhibit large regions of separated flow especially in the transonic Mach number range. The Saturn-Apollo launch vehicles are replete with flow separations of various types (Fig. 2-1). These have a dominating influence on the aerodynamic loading over the vehicle in the transonic and low supersonic speed range where the vehicle experiences maximum dynamic pressure, (Figs. 2-2 and 2-3).

The static loads can be determined by wind tunnel tests of a rigid model, and the buffeting force input from separated flow can also be assessed reasonably well from rigid-model wind tunnel tests. The remaining information needed for the evaluation of vehicle dynamics – the aerodynamic damping – is more difficult to obtain, however. To simulate elastic vehicle response in a wind tunnel test is a major undertaking. The model design and the test are extremely complicated, and the results of this expensive test may still be of limited value. Even if a satisfactory set of data is obtained, it may well be for an obsolete configuration. The complexity of the elastic model necessitates lead times of one-half to one year; and during that time the vehicle design is likely to have changed. Without any analytical means, the wind tunnel data cannot be applied to a new design.

These problems were recognized at the Marshall Space Flight Center in connection with the design of the Saturn-Apollo launch vehicles. As Lockheed had encountered similar problems on the Agena ascent vehicles, Lockheed Missiles & Space Company (LMSC) was engaged by the Marshall Space Flight Center in a consultant capacity to develop analytical means for prediction of full scale vehicle dynamics. The approach

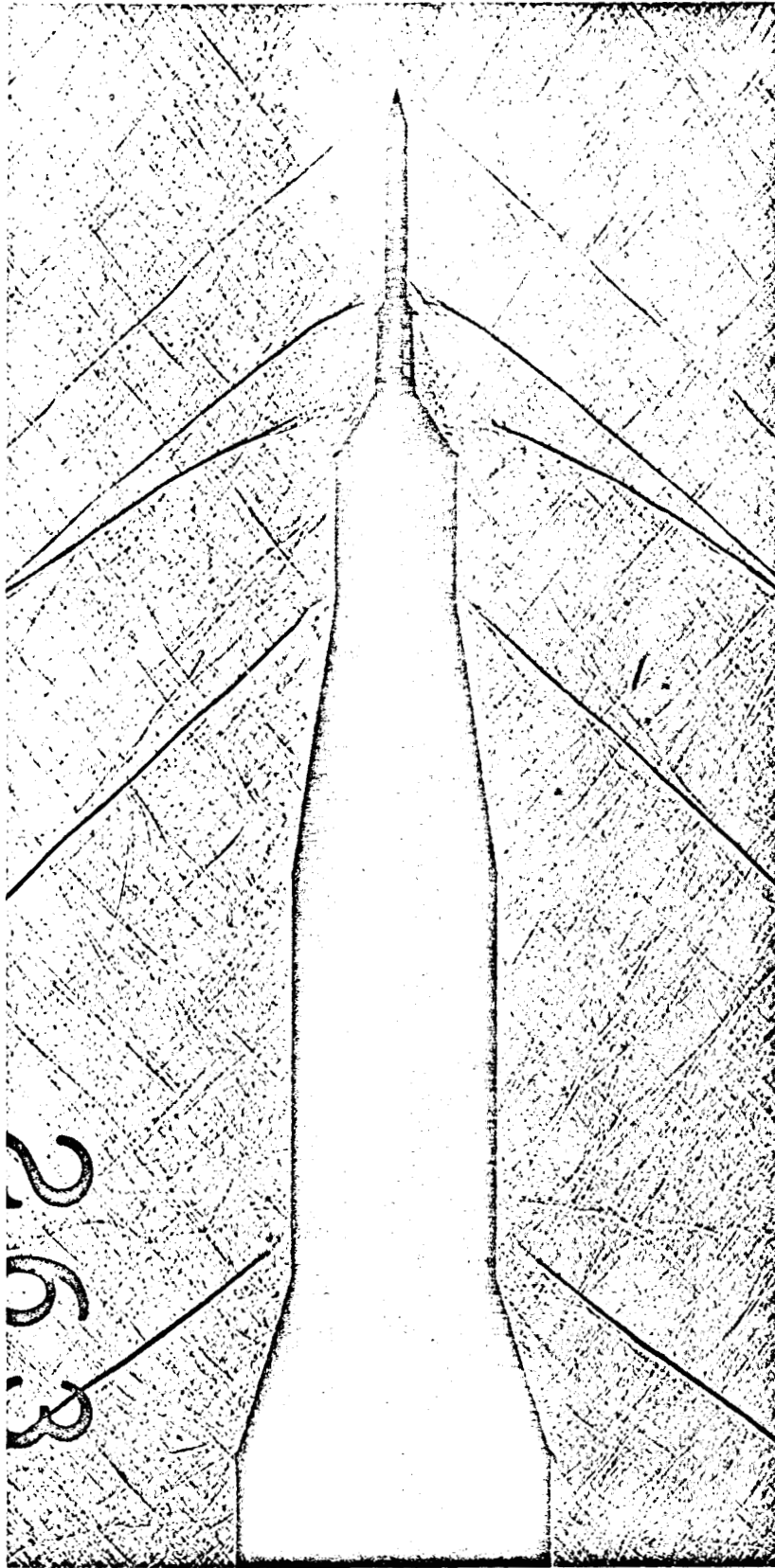


Fig. 2-1 Supersonic Flow Field on the Saturn-Apollo Launch Vehicle

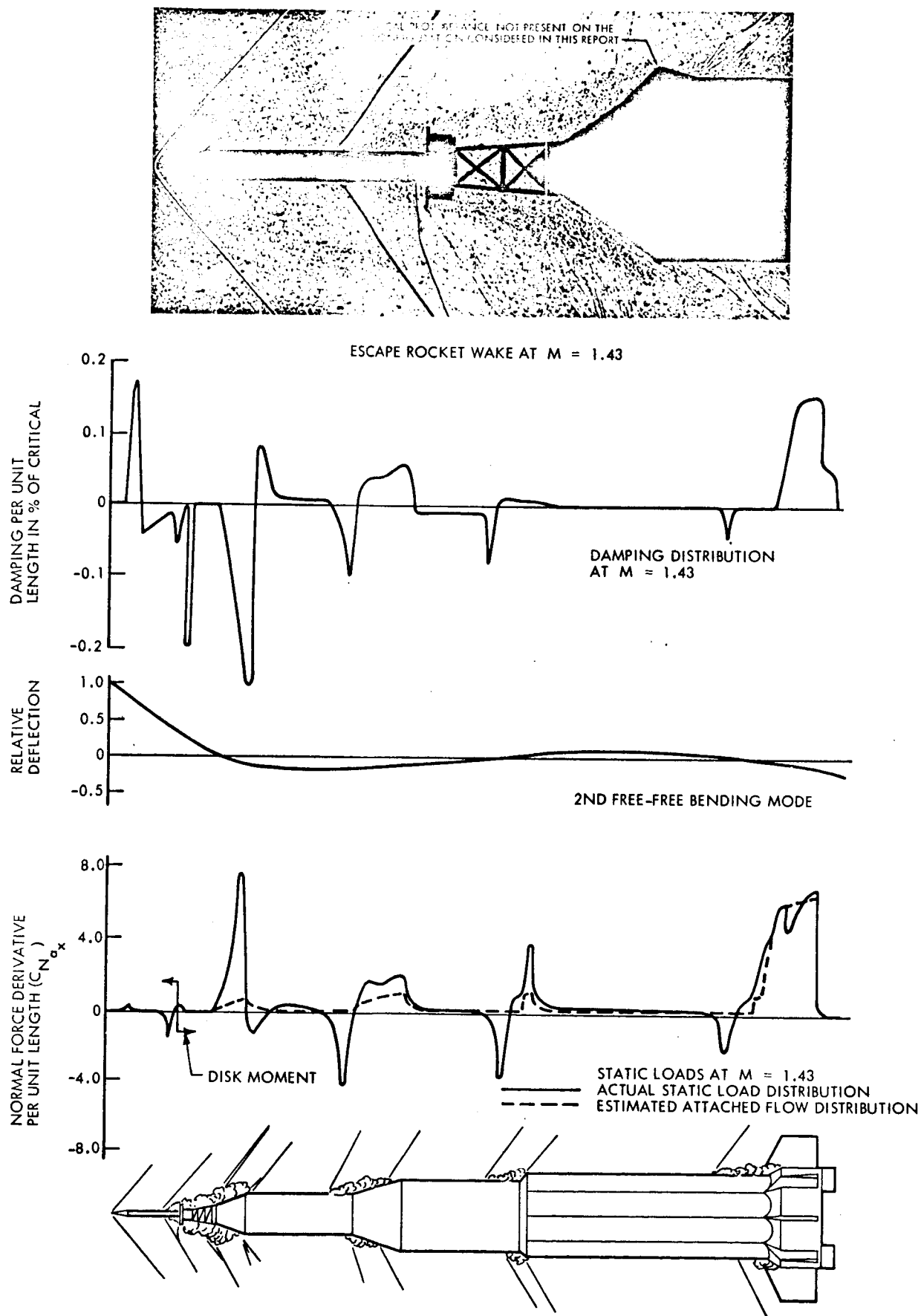


Fig. 2-2 Supersonic Static and Dynamic Loads on the Saturn Booster, ($\alpha = 0$)

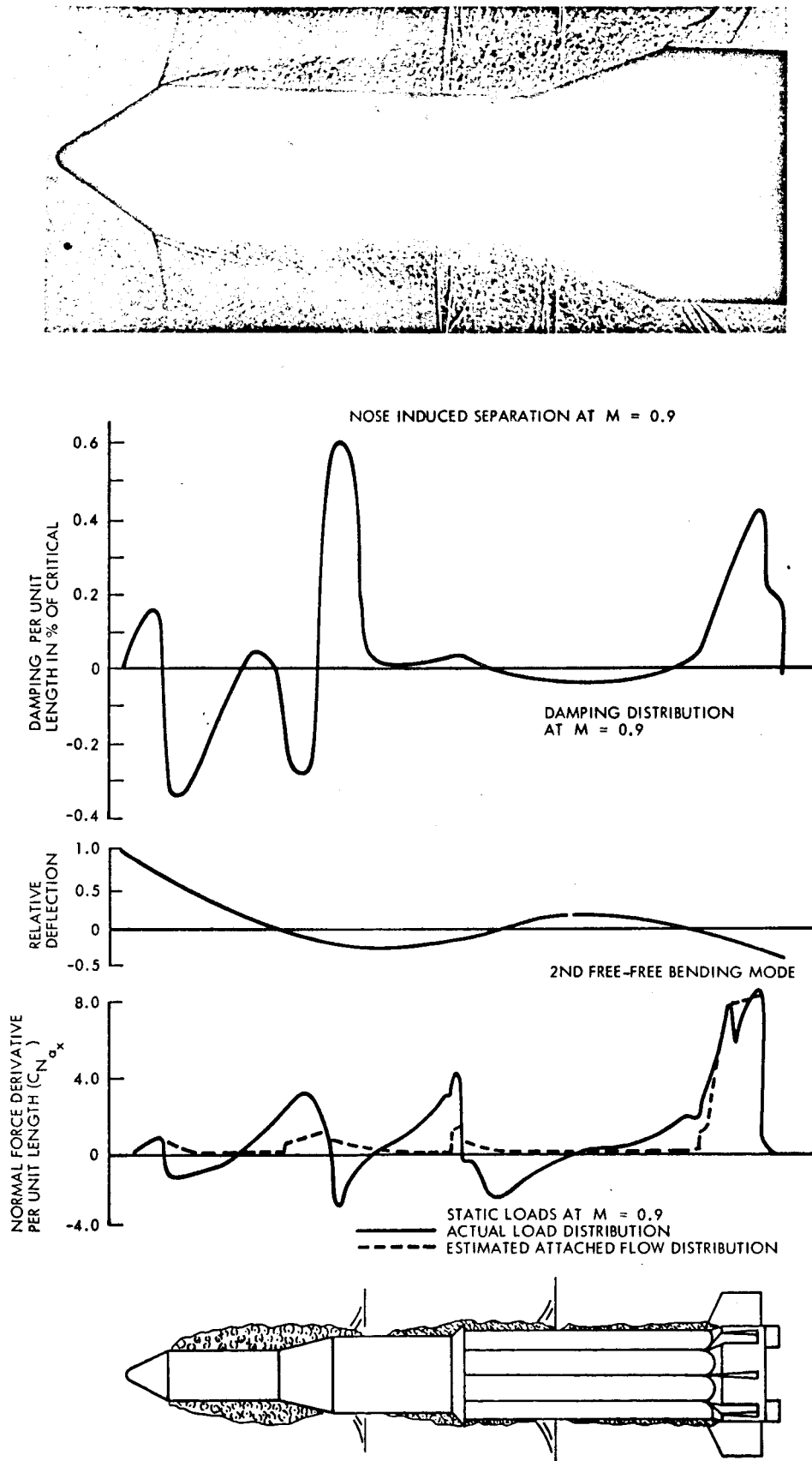


Fig. 2-3 Subsonic Static and Dynamic Loads on the Saturn Booster, Tower Off ($\alpha = 0$)

to the accomplishment of this ambitious task has been to study each of the different separated flow phenomena occurring on the Saturn-Apollo booster separately, developing analytical means of predicting the dynamic characteristics from experimental static characteristics. The progress of this work has been reported in detail in the following interim reports:

- "Steady Loads on Spiked Blunt Bodies of Revolution," (Ref. 1)
- "Separated Flow Effects on the Static Stability of Cone-Cylinder-Flare Bodies," (Ref. 2)
- "Static Loads on the Saturn I-Apollo Launch Vehicle," (Ref. 3)
- "Report on Saturn I-Apollo Unsteady Aerodynamics," (Ref. 4)
- "Static Pressures and Forces Generated by a Flow Separation Disk," (Ref. 5)
- "Unsteady Characteristics of a Spiked Bluff Body," (Ref. 6)
- "Forces Induced on Bodies in Free Wakes and Three Dimensional Cavities," (Ref. 7)
- "Separated Flow Effects on the Dynamic Stability of Blunt-Nosed Cylinder-Flare Bodies," (Ref. 8)

The present report is intended to provide a comprehensive summary of the results of the study illustrating two things in particular: (1) the main features of the different types of flow separation, and (2) the accuracy of quasi-steady predictions of dynamic data.

Section 3

STATEMENT OF PROBLEM

The loads occurring in a separated flow region fall generally into two categories. The most significant loading is caused by the effect that forebody attitude and relative displacement have on the flow separation, thus modifying the load on the submerged body. It is obvious that a time lag will occur between the instant the separation source (the forebody) is perturbed and the time the separated flow field has altered the submerged body loads. The time lag causes a phase shift in the dynamic case such that statically stabilizing loads become dynamically destabilizing. This time lag effect is greatly modified by structural or mechanical phasing. Thus, when a node of the bending body or the center of gravity (oscillation center) of the rigid body occurs between the separation source and the submerged body element, the time lag effect is greatly amplified, and moderately stabilizing static loads will cause drastically high undamping effects. The remainder of the load in the separated region is determined by the local attitude of the submerged body element. Dynamically, this load is dependent upon the instantaneous change in local attitude and displacement. This loading is, for large regions of separated flow, significantly smaller than the forebody-dependent time-lag-sensitive loading, and the latter will, therefore, dominate the separated flow contribution to the vehicle damping. Consequently, when a node or oscillation center is between separation source and submerged body element total reversal occurs, and statically stabilizing loads result in dynamically destabilizing loads, and vice versa.

The description of the dynamic effects of separated flow over blunt bodies proceeds as follows: first the quasi-steady analytic tools relating static and dynamic effects are described in utmost brevity and generality, referring all mathematical exercises to an appendix (Appendix C). Thereafter, the various types of flow separation occurring on the Saturn-Apollo boosters are discussed briefly. The characteristics of each type of flow separation are then discussed, starting with wake impingement and spike-induced separation, and followed by a discussion of nose-induced separation and shock-induced separation. Finally, the correlation between quasi-steady predictions and dynamic wind tunnel test results with an elastic model is examined.

Section 4

QUASI-STEADY ANALYSIS

Quasi-steady forces are essentially static forces modified to account for slow perturbations from the static (steady state) condition. The quasi-steady force can in coefficient form be expressed as the product of the static force derivative and an effective angle of attack suitably modified to account for the slow perturbations from the static value, that is

$$C_{N_{Q.S.}} = C_{N_{static}} + \widetilde{C_N} = C_N(\alpha_o) + C_{N_\alpha} \cdot \widetilde{\alpha} \quad (4.1)$$

In classical quasi-steady theory, $\alpha_o + \widetilde{\alpha}$ is the local instantaneous cross flow angle.

$$\alpha_o + \widetilde{\alpha} = \alpha_o + \theta + \frac{\dot{z}}{U} \quad (4.2)$$

where

- α_o = Trim angle of attack
- θ = Angular perturbation from α_o
- \dot{z} = Translatory velocity
- U = Vehicle velocity

This formulation is valid for aerodynamic forces only dependent upon local conditions. As was indicated earlier, this is only a small portion of the aerodynamic load on a body element submerged in separated flow. The main portion of the load is dependent upon upstream conditions at the separation source. One can express the separation-induced loading in the following form.

$$\Delta C_{N_{Q.S.}} = \Delta C_{N_{static}} + \widetilde{\Delta C_N} = \Delta C_N(\alpha_o) + \Delta C_{N_\alpha}(\widetilde{\alpha_i}) \quad (4.3)$$

The quasi-steady force N_S in coefficient form can be expressed as (see Appendix C):

$$\begin{aligned}\widetilde{C}_N(t) &= C_{N_{\alpha_S}} \alpha_S(t) \\ \Delta^i \widetilde{C}_N(t) &= \Delta^i C_{N_{\alpha}} \alpha_N(t - \Delta t) \\ &\quad + \Delta^i C_{N_{\beta}} \beta(t - \Delta t)\end{aligned}\tag{4.5}$$

where

$$\begin{aligned}\alpha_S(t) &= \theta(t) - (x_S - \bar{x}) \dot{\theta}(t)/U \\ \alpha_N(t - \Delta t) &= \theta(t - \Delta t) - (x_N - \bar{x}) \dot{\theta}(t - \Delta t)/U \\ \beta(t - \Delta t) &= \frac{x_N - \bar{x}}{x_N - x_S} \theta(t - \Delta t) - \frac{x_S - \bar{x}}{x_N - x_S} \theta(t)\end{aligned}$$

For slow oscillations

$$\begin{aligned}\theta(t - \Delta t) &\approx \theta(t) - \Delta t \dot{\theta}(t) \\ \dot{\theta}(t - \Delta t) &\approx \dot{\theta}(t) - \Delta t \ddot{\theta}(t) \approx \dot{\theta}(t)\end{aligned}\tag{4.6}$$

Thus $\alpha_S(t)$, $\alpha_N(t - \Delta t)$, and $\beta(t - \Delta t)$ become simply

$$\begin{aligned}\alpha_S(t) &= \theta(t) - (x_S - \bar{x}) \dot{\theta}(t)/U = \theta(t - \Delta t_S) \\ \alpha_N(t - \Delta t) &= \theta(t) - \Delta t \dot{\theta}(t) - (x_N - \bar{x}) \dot{\theta}(t)/U \\ &= \theta(t - \Delta t - \Delta t_N)\end{aligned}$$

$$\begin{aligned}
 \beta(t - \Delta t) &= \frac{x_N - \bar{x}}{x_N - x_s} \theta(t) - \frac{x_N - \bar{x}}{x_N - x_s} \Delta t \dot{\theta}(t) - \frac{x_s - \bar{x}}{x_N - x_s} \theta(t) \\
 &= \frac{x_N - \bar{x}}{x_N - x_s} \theta(t - \Delta t) - \frac{x_s - \bar{x}}{x_N - x_s} \theta(t)
 \end{aligned} \tag{4.7}$$

where

$$\begin{aligned}
 \widetilde{\Delta t}_s &= (\xi_s - \bar{\xi}) c/U \\
 \widetilde{\Delta t}_N &= (\xi_N - \bar{\xi}) c/U \\
 \Delta t &= (\xi_N - \xi_s) c/\bar{U} \\
 \bar{U} &\leq U \\
 \xi &= x/c
 \end{aligned}$$

In Eq. (4.5) Δt is a true time lag and is always positive, its magnitude being dependent upon the mean velocity, \bar{U} , with which the effects of cross flow changes at x_N are communicated through the separated flow down to the submerged body element at x_s . The quantities $\widetilde{\Delta t}_s$ and $\widetilde{\Delta t}_N$ are generalized time lags corresponding to the effect of mechanical or structural phasing. That is, for the \bar{x} location shown in Fig. 4-1, both $\widetilde{\Delta t}_s$ and $\widetilde{\Delta t}_N$ are positive, representing lag effects. In other words, the negative crossflow angles, $-(x_s - \bar{x}) \dot{\theta}/U$ and $-(x_N - \bar{x}) \dot{\theta}/U$, induced by the pitch velocity oppose the crossflow angle θ due to body attitude. Thus, the resultant crossflow angle lags the body attitude. The effective time increment of this lag is $\widetilde{\Delta t}_N$ at x_N and $\widetilde{\Delta t}_s$ at x_s . When the oscillation center is forward of x_s and x_N , the pitch velocity crossflow amplifies the attitude angle, thus causing the resultant crossflow to lead the body attitude.

Generalizing further, the force components in Eq. (4.5) that contribute dynamically, i. e., affect the damping, can all be expressed through the following equation.

$$\widetilde{C_F}(t) = C_{F_\alpha} \theta(t - \tau) \quad (4.8)$$

$$\tau = \Delta t + \widetilde{\Delta t}$$

When τ is positive, static and dynamic stability effects are of opposite sign, as is illustrated by Fig. 4-2.

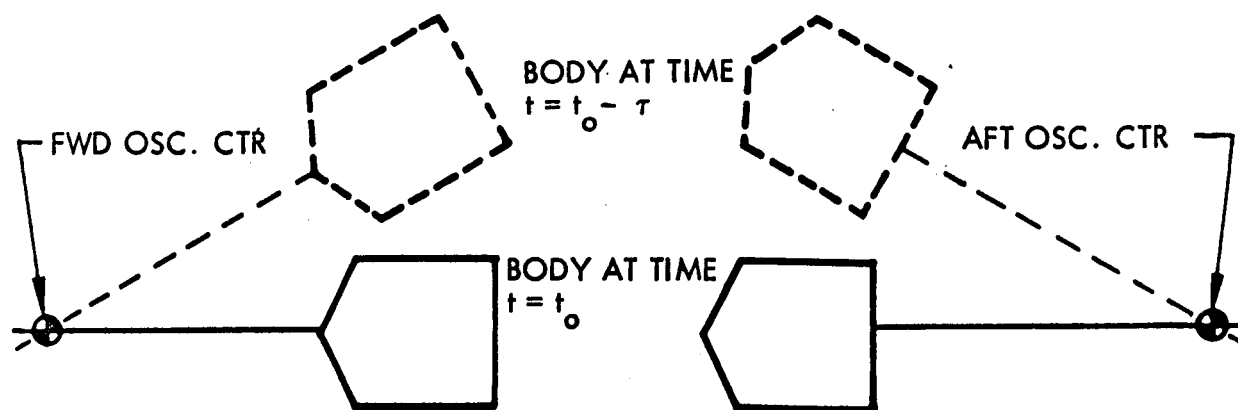
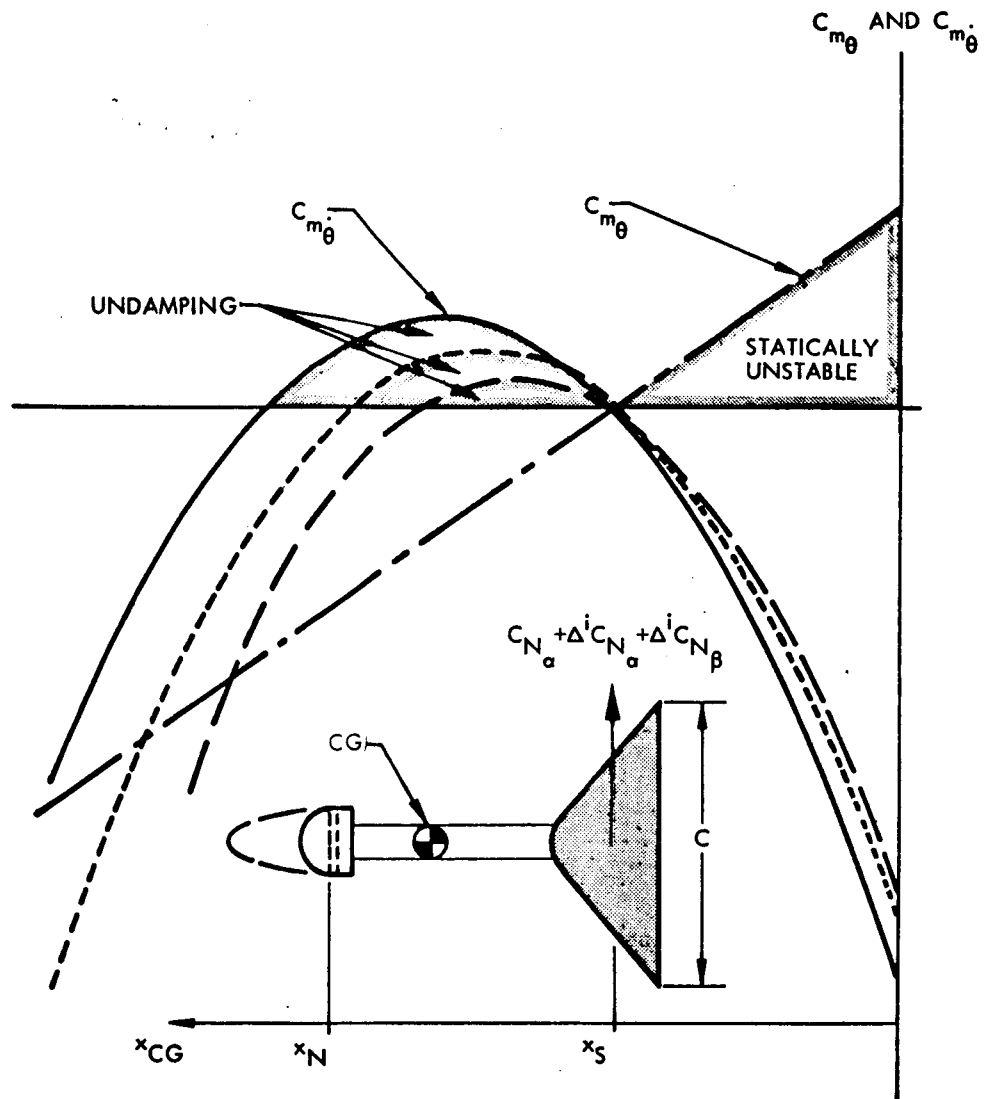


Fig. 4-2 Dynamic Time Lag Effects

When the body comes down to zero angle of pitch at time $t = t_0$, it has a residual force generated at the earlier time $t = t_0 - \tau$. For the forward oscillation center, where the body force is statically stabilizing, the residual force will be negative, thus accelerating the pitching motion. That is, the body force is undamping (dynamically destabilizing). For the aft oscillation center the effects are the opposite, i. e., the body force is statically destabilizing but dynamically stabilizing (damping).

This reversal between static and dynamic effects is especially drastic when the mechanical phase lag $\widetilde{\Delta t}$ adds to the true time lag Δt . Figure 4-1 and Eq. (4.5) show that $\widetilde{\Delta t}_N$ adds lag when the oscillation center is aft of the separation source, i.e., when $\bar{x} < x_N$. It was shown earlier by use of Fig. 4-2 that the effects were un-damping for oscillation centers forward of the submerged body, i.e., for $\bar{x} > x_s$, and damping for aft oscillation centers, $x < x_s$. Thus, the dramatic change from static stability to large dynamic instability occurs when the oscillation center is located between the separation source and the submerged body. This is illustrated in Fig. 4-3 which shows the effect that the location of the oscillation center has on the dynamic and static stability of the submerged body. Three different separation sources are considered. The disk produces a wake aligned with the free stream, i.e., the effect of α_N is zero, $\Delta^i C_{N\alpha} = 0$, and the translatory derivative, $\Delta^i C_{N\beta}$, is the only wake-induced effect. The blunt wake source produces separated flow ahead of its base and directs the wake upwards adding $\Delta^i C_{N\alpha} > 0$ to the pure translatory derivative $\Delta^i C_{N\beta}$. A slender wake source directs the wake initially along its centerline and thus downward from the free-stream direction, producing a negative force derivative $\Delta^i C_{N\alpha} < 0$. For comparison purposes, the total wake-induced derivative $\Delta^i C_{N\alpha} + \Delta^i C_{N\beta}$ is held constant so that the different wake sources produce identical static stability effects. The results shown in Fig. 4-3 thus illustrate how the reversal from static stability to dynamic instability is increasingly worse when the wake source is changing from a slender ogive (or cone) via a disk shape to a blunt ogive. The escape rocket disk on the Saturn-Apollo launch vehicle produces this effect for the second bending mode where the forward nodal point is located between the escape rocket and the command module (Fig. 2-2).



$$C_{N_{\alpha}} = 1$$

$$\Delta^i C_{N_{\alpha}} + \Delta^i C_{N_{\beta}} = 10$$

$$\Delta^i C_{N_{\alpha}} = \begin{cases} 0 & \text{Disk Wake Source} \\ 3 & \text{Blunt Wake Source} \\ -3 & \text{Slender Wake Source} \end{cases}$$

$$\text{Ref. Area} = \frac{\pi C^2}{4}$$

Fig. 4-3 Wake-Induced Dynamic Effects for Various Oscillation Centers

Section 5

DISCUSSION OF RESULTS

The separated flow produced by the escape rocket on the Saturn-Apollo launch vehicle (Fig. 2-2) drastically alters the aerodynamic loads on the command module. Figure 5-1 shows how the flow separation reduces the forebody axial force at $\alpha = 0$ while substantially increasing the normal force derivative. The latter effect results from translating the wake over the submerged body, thus exposing the windward side to rapidly increasing velocities, and the leeward side to reduced velocities. This wake movement also generates a statically stabilizing axial force moment (force-couple). The similar wake produced by a spike, Fig. 5-2, shows that the wake-translating effect dominates. The wake-translating effects of α and of spike deflection angle β should be the same, since the relative spike deflection is the same ($z = \alpha L = \beta L$ for small angles). Thus, the small difference between α - and β -characteristics is due to rotating the submerged body through the angle α . That is, the local crossflow attitude effect $C_{N_{\alpha s}}$ is small compared to the force derivative $\Delta^i C_{N_{\beta}}$ induced by the wake movement.

The translatory derivative $\Delta^i C_{N_{\beta}}$ is proportional to the separation-induced drag reduction at $\alpha = 0$ (Ref. 1). The spike length giving the maximum drag reduction on a hemisphere-cylinder body is shown in Fig. 5-3 as a function of Mach number. The large difference in minimum drag between turbulent and laminar reattaching wakes is also illustrated. When the spike length deviates from the optimum length, less drag reduction is achieved (Fig. 5-4). The decrease in drag reduction for shorter spikes can be normalized in the way shown to eliminate the effect of Mach number, thus providing a means of predicting spiked body drag. (An orderly weak influence of the basic nose shape has been absorbed in the error band shown without distinction from the pure data scatter.) When the spike is made longer than the optimum length, retarded spike separation occurs producing increased drag due to the fact that the boundary layer at separation now is turbulent and produces a higher plateau pressure (in the "dead-air" region).

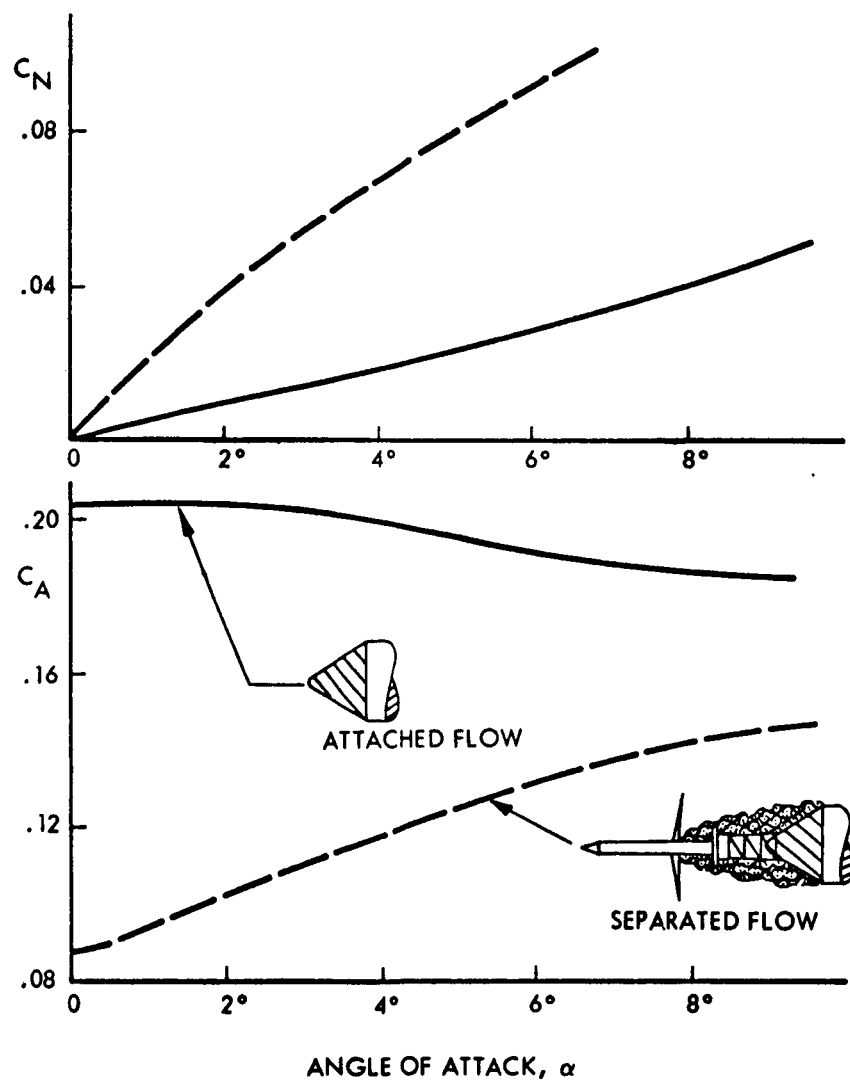


Fig. 5-1 Effect of Escape Rocket on Apollo Command Module Forces at $M = 1.0$

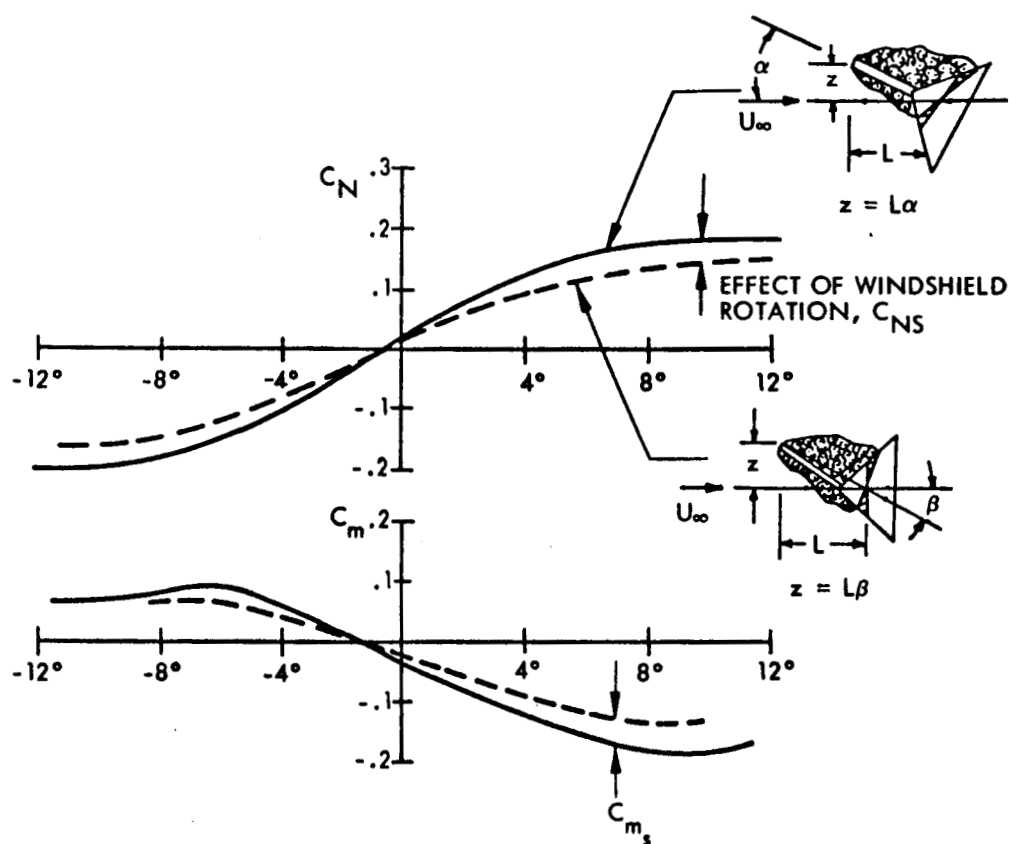


Fig. 5-2 Comparison of Angle of Attack and Spike Deflection Effects

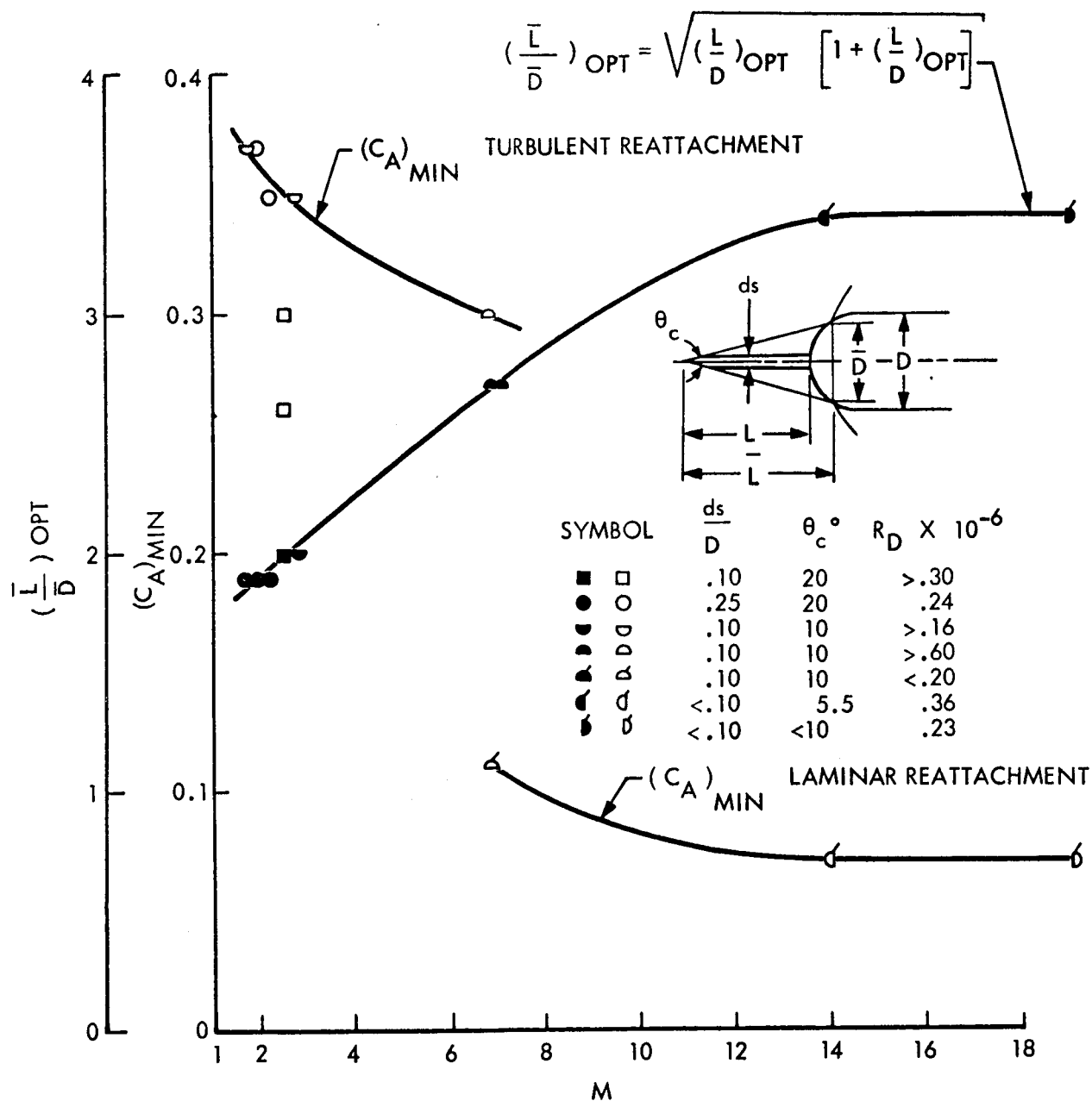


Fig. 5-3 Optimum Spike Length and the Associated Minimum Forebody Drag on a Hemisphere-Nose Body at Supersonic and Hypersonic Mach Numbers

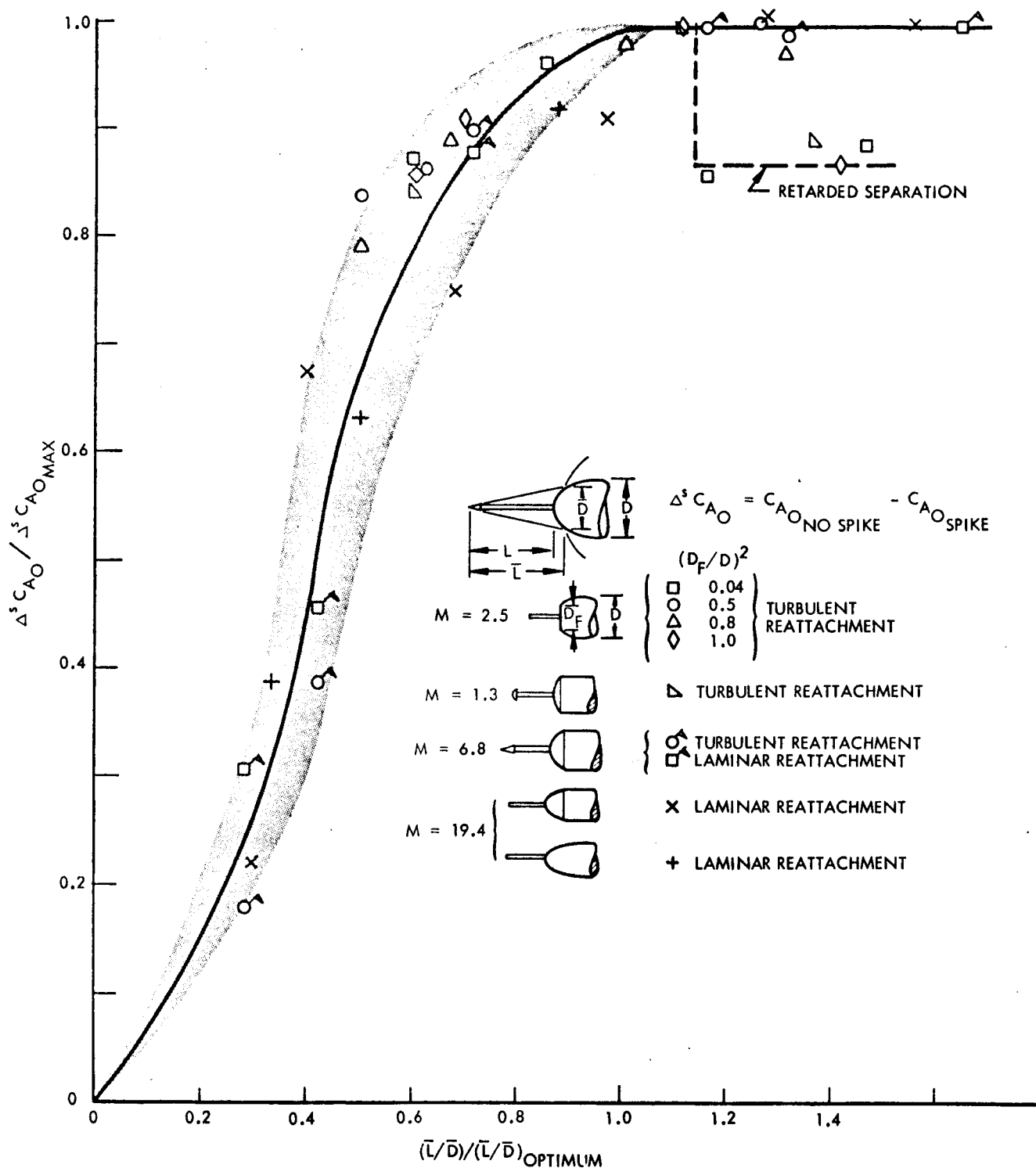


Fig. 5-4 Relative Loss in Drag Reduction for Non-Optimum Spike Length

Retarded separation on a thick spike is essentially the flow pattern produced by a disk, such as on the escape rocket in Fig. 2-2. Analysis of data for disk-induced separation (Ref. 5) shows that the axial force couple induced on the disk by the wake movement is a dominating aerodynamic characteristic, at least at moderate supersonic Mach numbers when the lifted boundary layer (free shear layer) is not excessively thick (Fig. 5-5). Then the high velocity portions in the shear layer produce large pressure increases on the rim of the disk. A slight movement of the separation, such as occurs at low angles of attack, produces a drastic change in the axial forces and associated pitching moment on the disk (illustrated in the inset in Fig. 5-5). The separation region is greatly increased on the leeward side and slightly decreased on the windward side due to forebody crossflow effects on the boundary layer approaching separation. The analogous situation exists in the shock-induced separated flow regions ahead of conical frustums on cylindrical bodies, as will be discussed later. In the dynamic case a true time lag exists, as the forebody crossflow changes have to be transmitted downstream to affect the separation and the disk loading.

Thus, as was shown in the previous section, one can expect large undamping effects from the statically stabilizing axial force moment induced on the disk face (Fig. 5-6). In addition, the negative forebody angle of attack induced by the pitching velocity also adds phase lag. The band shown represents the scatter in the experimental dynamic data as well as the upper and lower bounds predicted by quasi-steady theory (Ref. 6). At $M = 5$ and higher Mach numbers the induced axial force moment is reduced to the same order of magnitude as the normal force moment (Fig. 5-5) and can no longer drive the body dynamically unstable (Fig. 5-6). The undamping peak shown in Fig. 2-2 is the dynamic effect of the separation-induced axial force couple on the escape rocket disk.

The axial force deficit on a body, submerged in the wake from another body or in the separated flow region created by a spike, furnishes an important clue for the determination of the average convection velocity, \bar{U} , as well as of the local crossflow effect, $C_{N_{\alpha S}}$. Defining a mean dynamic pressure deficit from the axial force deficit gives the following estimates of \bar{U} and $C_{N_{\alpha S}}$.

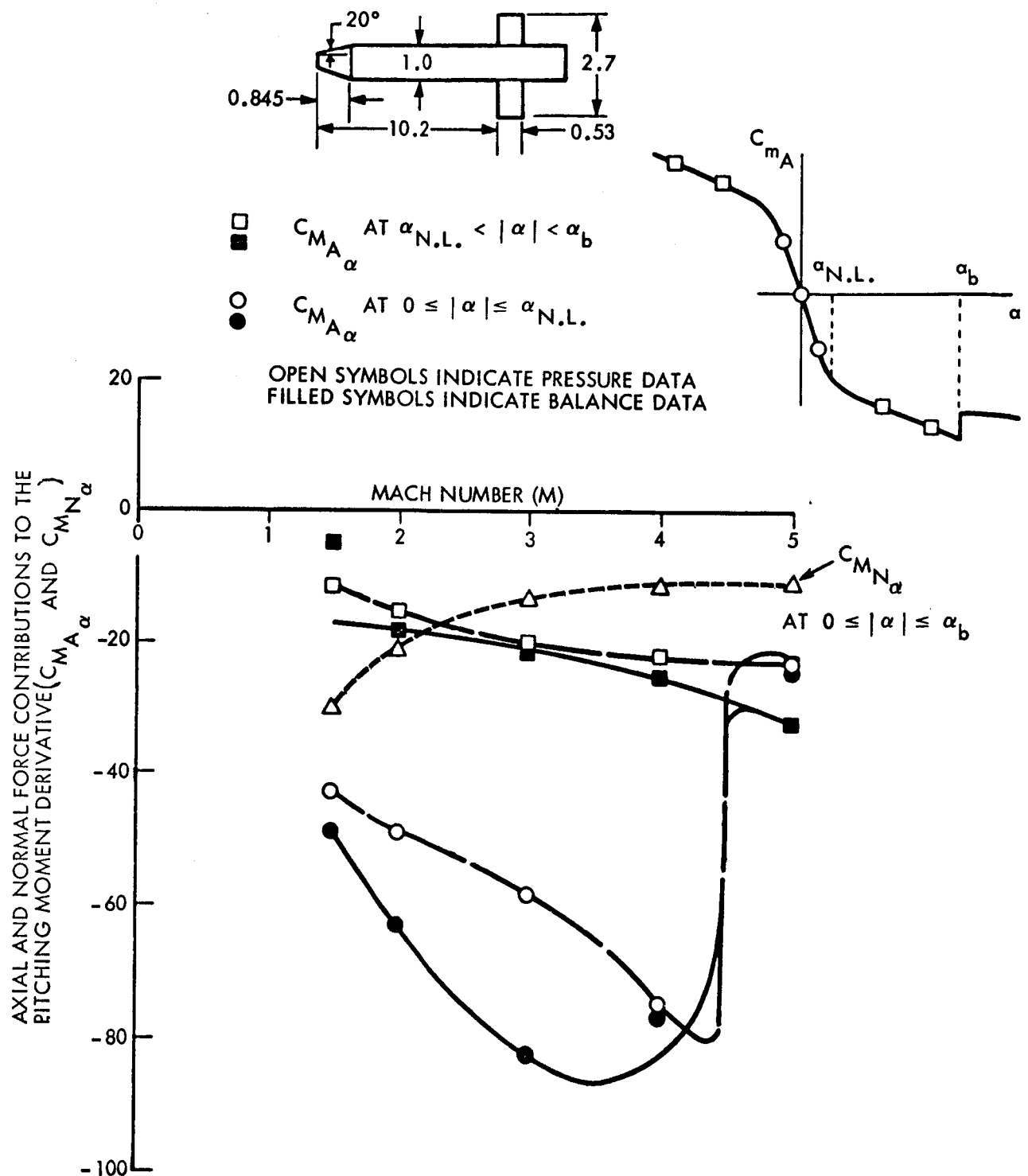


Fig. 5-5 Static Stability Effects of a Flow Separation Disk at Supersonic Mach Numbers

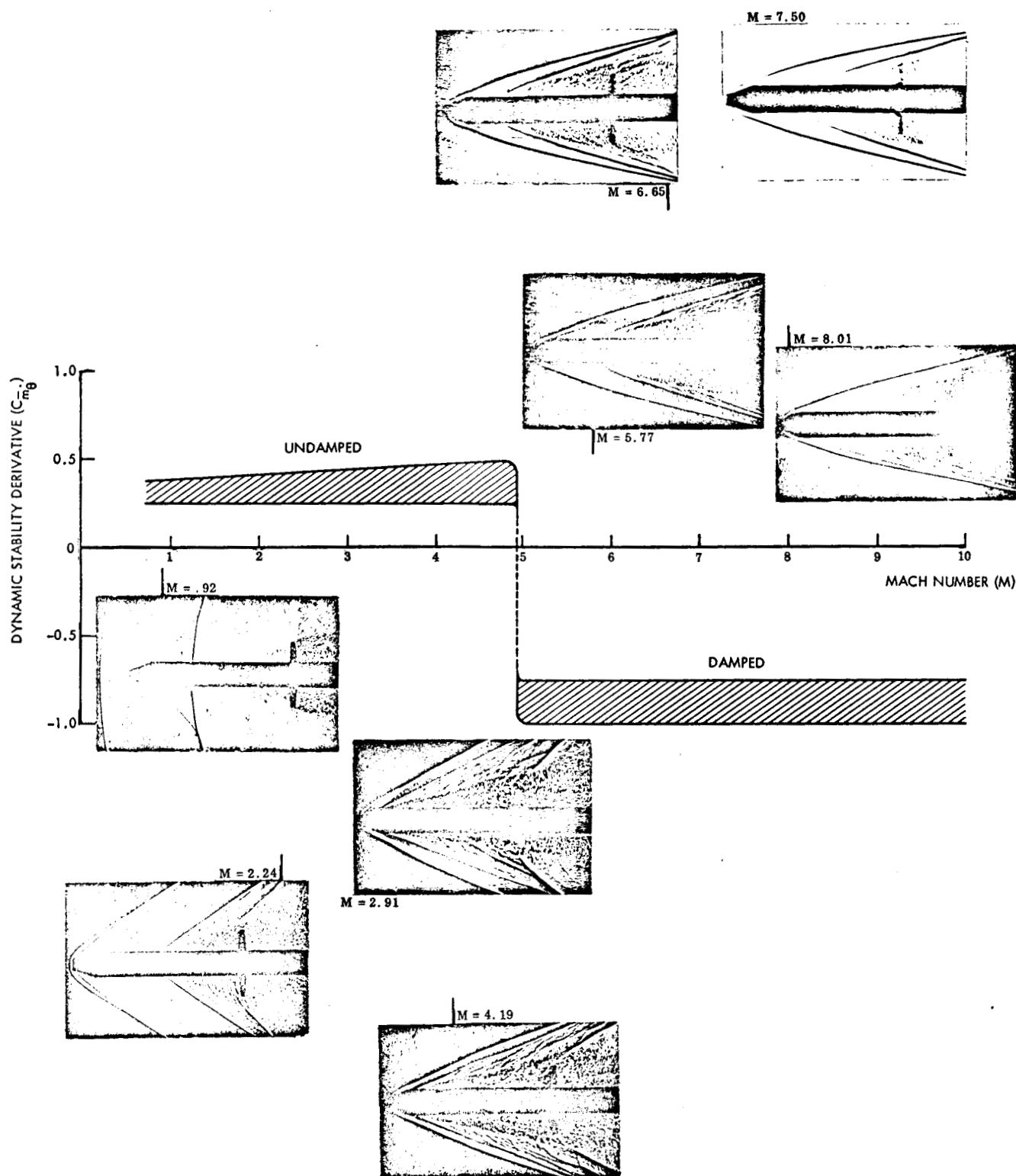


Fig. 5-6 Separated Flow Pattern and Pitch Damping of a Cylindrical Body With a Flow Separation Disk

$$\bar{U}/U = \left[\left(C_{A_o} \right)_s / \left(C_{A_o} \right)_a \right]^{1/2} \quad (5.1)$$

$$C_{N_{\alpha_s}} = \left[\left(C_{A_o} \right)_s / \left(C_{A_o} \right)_a \right] \cdot C_{N_{\alpha_a}} \quad (5.2)$$

where

$\left(C_{A_o} \right)_s$ = forebody axial force of the body submerged in the separated flow
(at $\alpha = 0$)

$\left(C_{A_o} \right)_a$ = forebody axial force in attached flow (at $\alpha = 0$)

$C_{N_{\alpha_a}}$ = body normal force derivative in attached flow

The veracity of using the axial force reduction to compute the local crossflow effect has been investigated experimentally (Ref. 7). As indicated by the data in Fig. 5-7, the method appears to be good for a wake source distance of 1/2 a caliber (base diameter of submerged body) and for 2 calibers distance or more. For intermediate distances, rotation of the submerged body pushes the wake further to the leeward side creating additional normal force. Judging by the shadowgraphs in Fig. 5-7 this occurs when the wake closes (necks) on the submerged body. When the body is closer to the wake source, the wake opens up, and reattachment occurs aft of the body shoulder, so that body rotation has negligible effect on the wake configuration. When the body is moved aft of the wake neck, (see $M = 1.96$ shadowgraph in Fig. 5-7), the upstream communication is effectively cut off. When the submerged body is located in the wake neck, however, any change of the reattachment conditions, e.g. through local angle of attack, alters the wake geometry. In order to affect the wake, the submerged body must affect conditions at the wake source. The wake source base-pressure should register this upstream influence, and does, as is confirmed by the data in Fig. 5-8. There is a very good correlation between the overeffectiveness of local crossflow, $C_{N_{\alpha_s}}$, and the sensitivity of the wake-source base-pressure to the same crossflow, $\partial C_{p_{bw}} / \partial \alpha_s$.

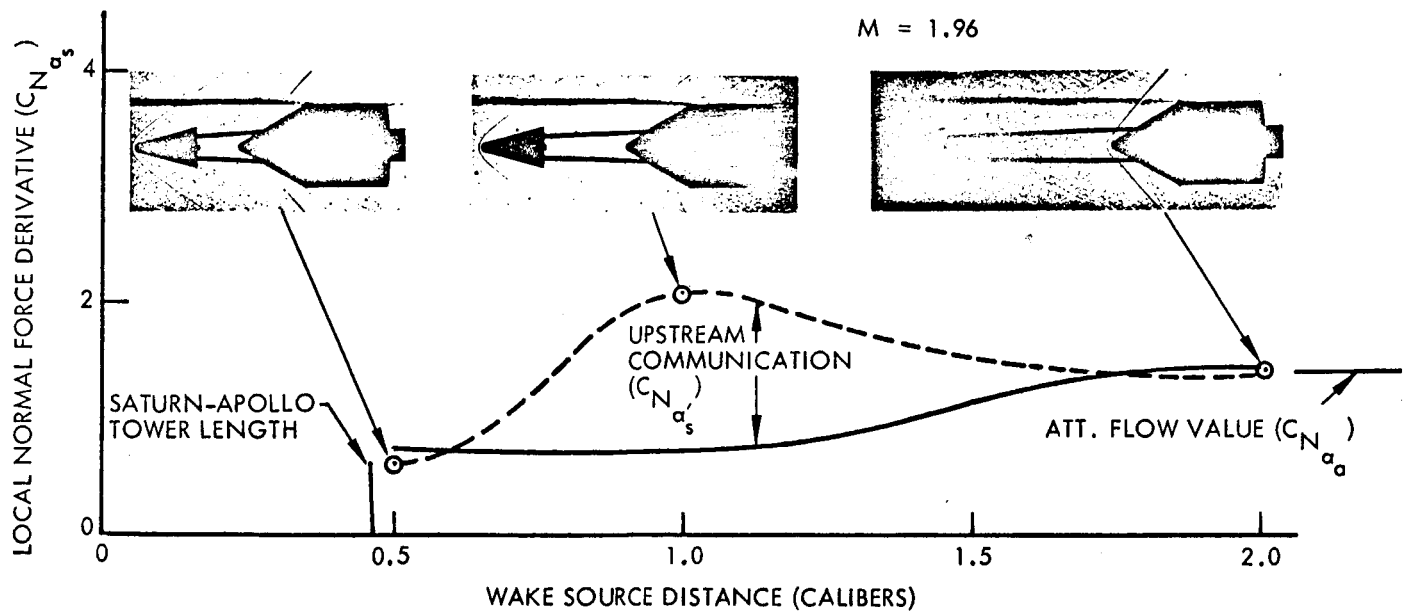
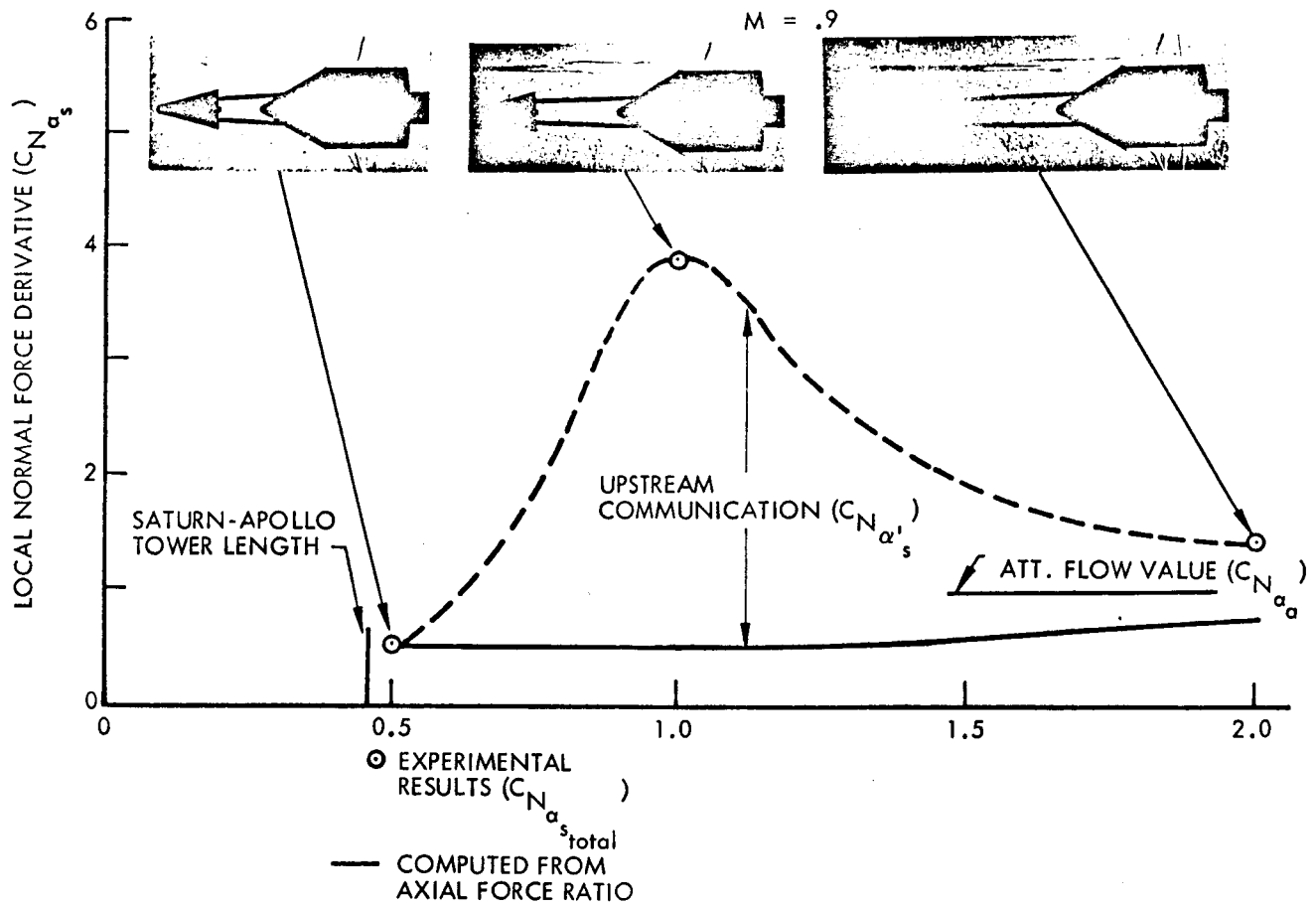


Fig. 5-7 Local Crossflow Effect on the Submerged Body (Directing Wake Source)

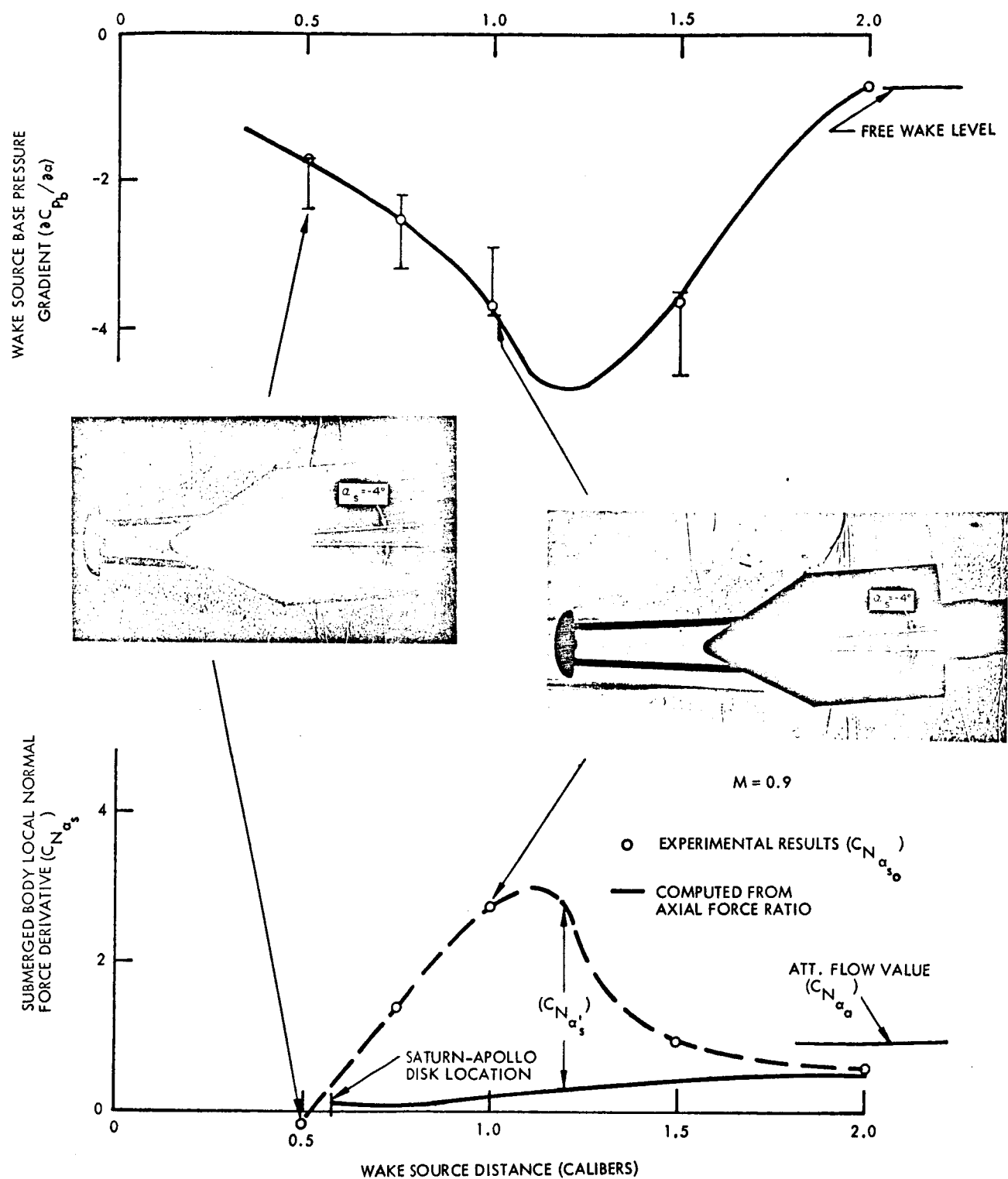


Fig. 5-8 Correlation Between Wake Source Base Pressure Sensitivity and Submerged Body Local Loads. (Non-Directing Wake Source)

When the reattachment on the submerged body is changed by translating the wake over the body, a similar upstream communication occurs increasing the translatory derivative $\Delta^i C_{N\beta}$ by an amount $\Delta^i C_{N\beta}'$ as shown in Fig. 5-9. The wake directing effect of the wake source is similarly amplified, the blunt ogive shape having its positive normal force derivative increased by $\Delta^i C_{N\theta_w}$ and the slender shape producing a negative force derivative increased in magnitude by an amount $\Delta^i C_{N\theta_w}'$, as illustrated by the data in Fig. 5-10.

The wake source distances corresponding to the two different escape rocket geometries of the Saturn-Apollo launch vehicle are indicated in Figs. 5-7 through 5-10. It is evident that the upstream communication effect is nonexistent for those distances, and that Eqs. (5.1) and (5.2), simple as they are, satisfactorily predict the characteristics of the Saturn-Apollo escape rocket wake (Fig. 5-11). Further research is needed, however, to resolve the dynamic behavior of wakes that have strong upstream communication effects.

When the escape system is removed, the blunt Apollo command module causes so-called nose-induced separation at high subsonic speeds (Fig. 2-3). The pressure is constant in the separated flow region extending to the aft service module and flare, where the reattachment process occurs (Fig. 5-12). At angle of attack, the thinned and strengthened windward side boundary layer can, aided by the increased constraint from the external flow, withstand a higher adverse pressure gradient. This permits the windward side pressures to approach attached flow values. On the leeward side, the effect is opposite but much less drastic. The nose-induced separation has plagued the missile industry for quite some time by producing dynamic instability and limit-cycling behavior of blunt-nosed reentry bodies at transonic speeds (Ref. 8). For practical reasons (shortness and maximum enclosed volume), the blunt noses have often an ogive shape. The separation pattern and its effect on body pressures and forces are, however, very much the same as for the body with conical nose-geometry (compare Figs. 5-12 and 5-13). The separation drastically alters the pressure and load distribution, and produces corresponding dramatic changes of the pitching moment. The data shown in

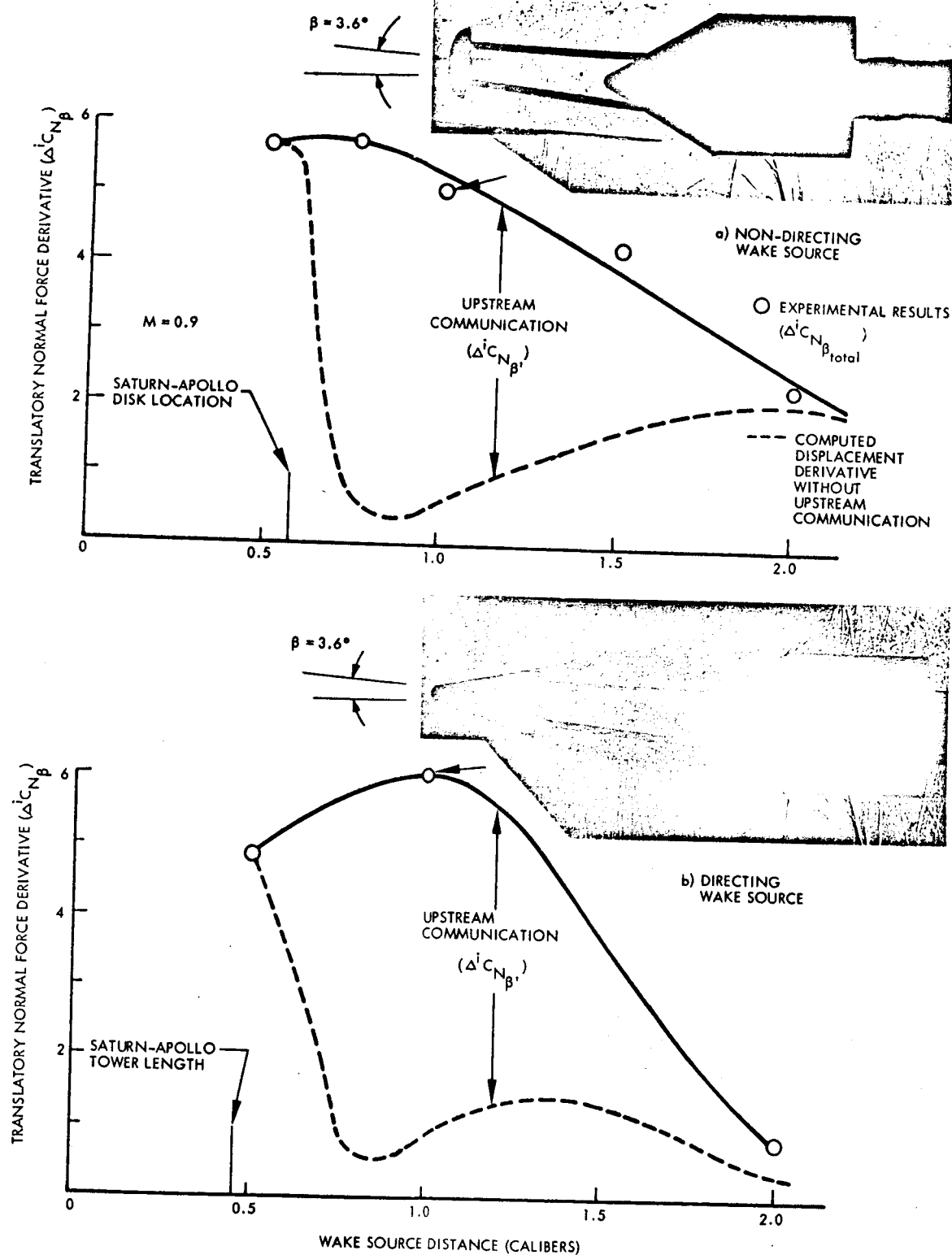


Fig. 5-9 Wake Translation Effects on the Submerged Body (Directing and Non-Directing Wake Sources)

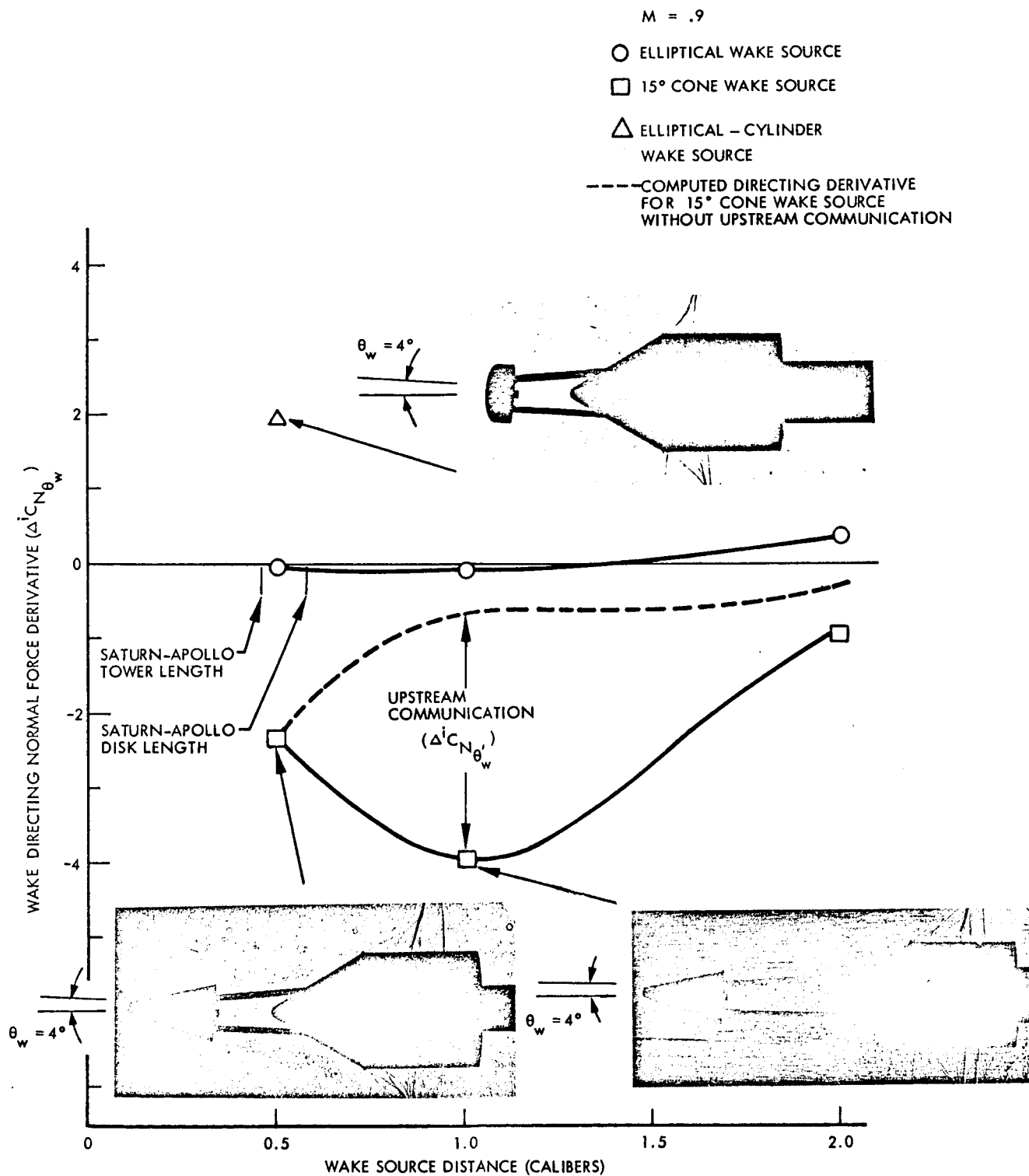


Fig. 5-10 Comparison of Wake Source Directing Effects

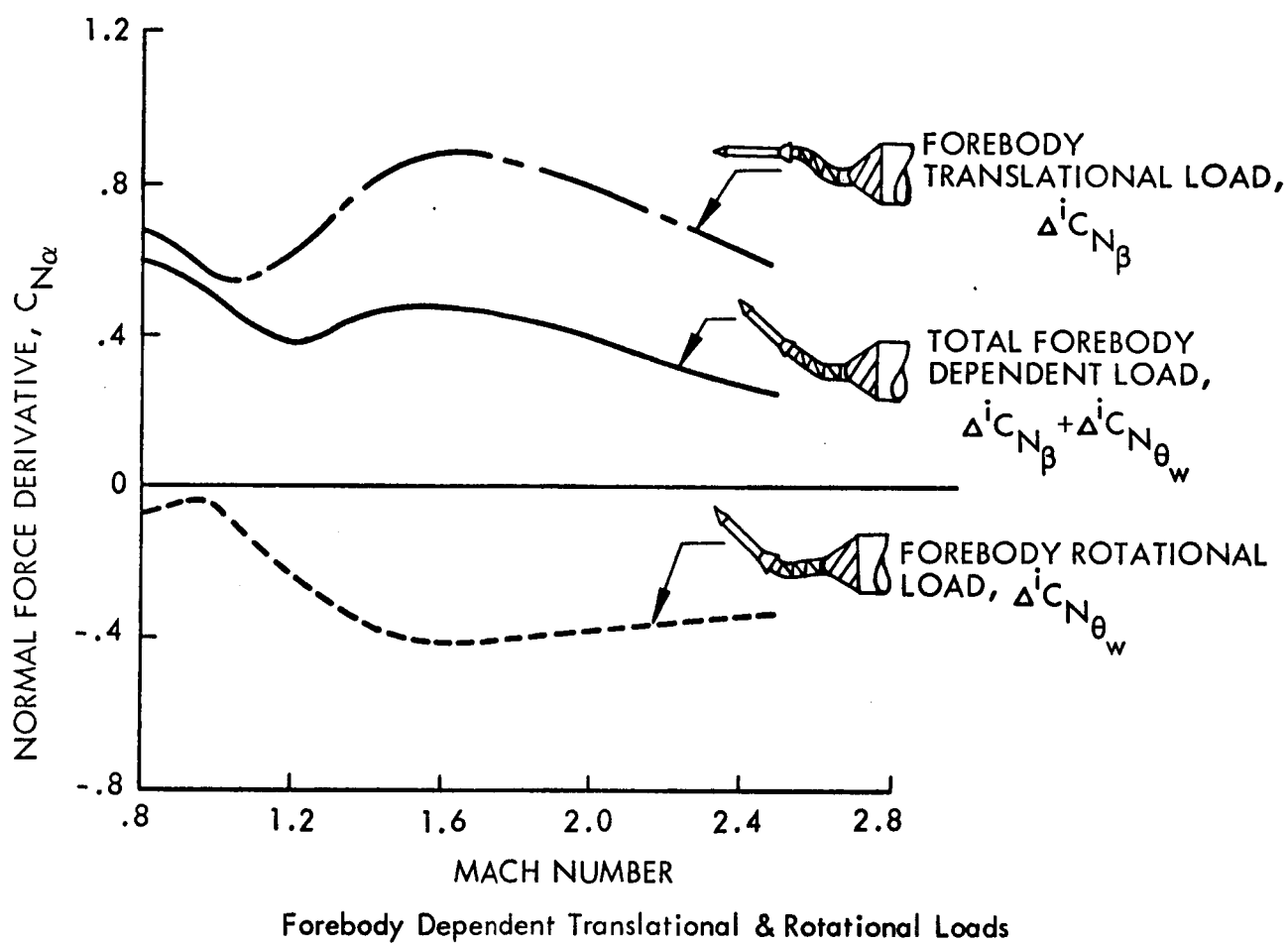


Fig. 5-11 Induced Forces on the Apollo Command Module by the Wake From the Disk-Off Escape Rocket

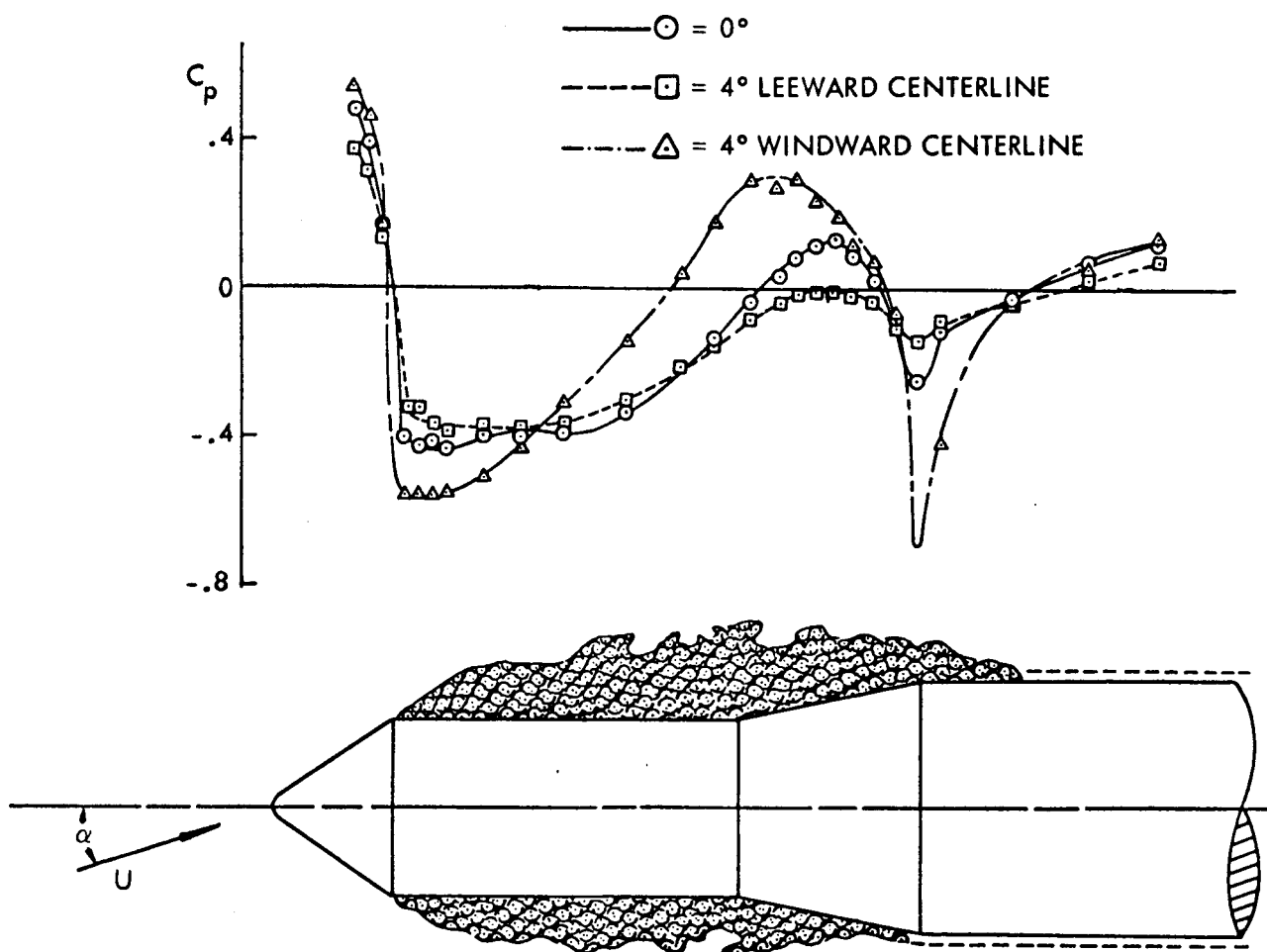


Fig. 5-12 Saturn Forebody Pressure Distribution With Escape System Removed at $M = 0.9$

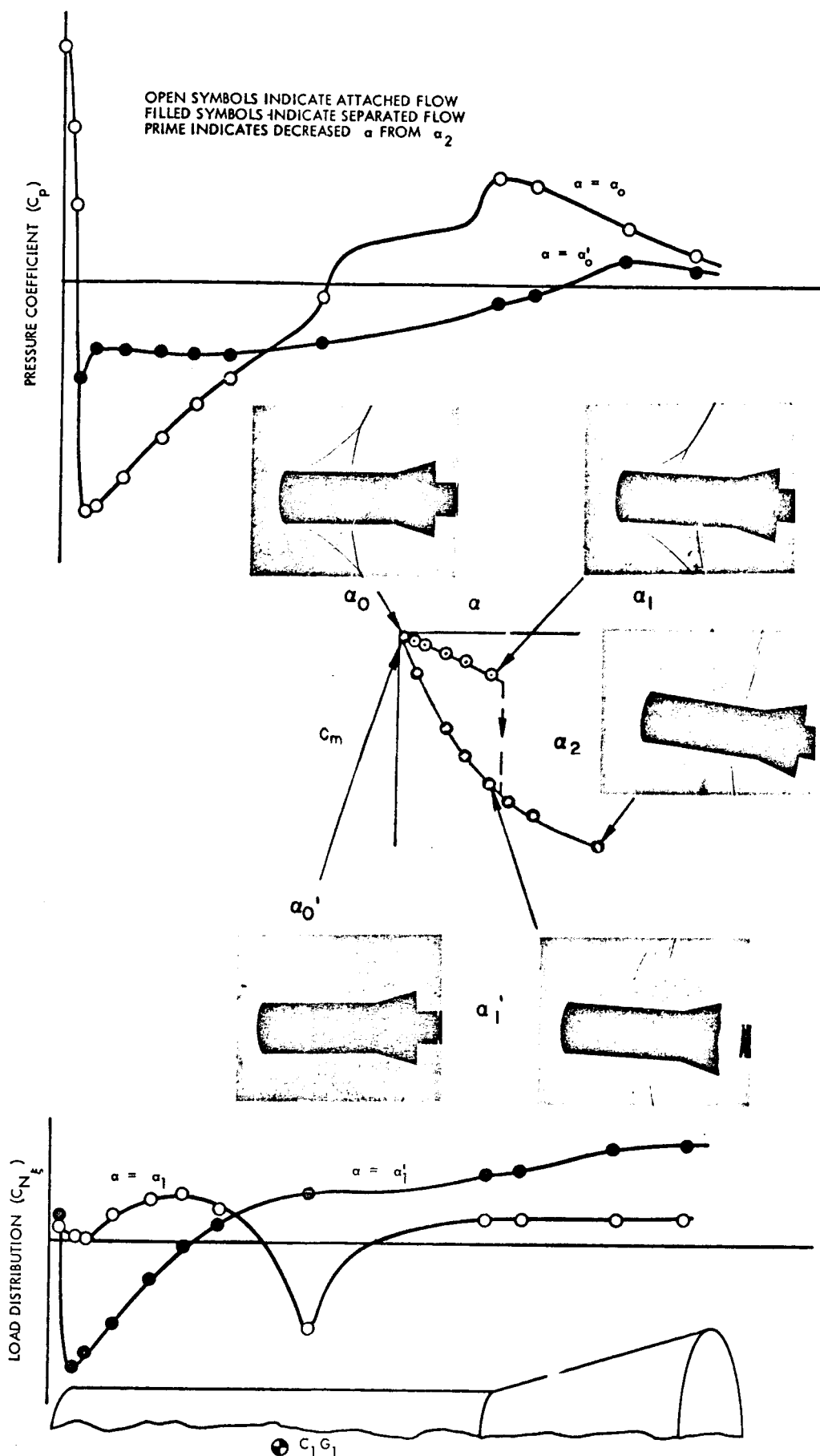


Fig. 5-13 Effect of Nose-Induced Separation on Pressure and Load Distribution Over a Blunt-Nose Cylinder-Flare Body

Fig. 5-13 are for very special test conditions where the flow is attached initially, but when a certain angle of attack (α_d) is exceeded nose-induced separation occurs and persists from there on, (at all angles of attack) until the Mach number is increased.

The effect of the nose-induced separation is to produce large static stability at low angles of attack. This is predominantly caused by the flare loading. The separation is directed by forebody crossflow at the nose shoulder. Thus, as described earlier, one can expect a correspondingly large undamping effect due to the time lag effect with mechanical phase lag added to the true time lag for all reasonable CG locations. This is confirmed by the data in Fig. 5-14, which also show that the quasi-steady predictions agree remarkably well with the experimental dynamic data, considering the appreciable data scatter. At higher angles of attack, the windward side has essentially attached flow and the leeward side is in a low velocity (dead air) region (see shadowgraphs in Fig. 5-13). Thus, the separated flow effects essentially disappear, and small amplitude oscillations will be damped at large trim angles of attack as illustrated in Fig. 5-15. Finite amplitude oscillations around zero angle of attack will be undamped for amplitudes below a certain value, and be damped for larger amplitudes. That is, the end result is steady oscillations at the limit cycle amplitude. The damping factor, $C_{\dot{m}\dot{\theta}}$, used in Fig. 5-15 to demonstrate this nonlinear amplitude effect, is the equivalent linear coefficient-effective damping derivative—defining the correct amount of energy dissipation per cycle. How this effective damping can be computed for various types of nonlinearities induced by separated flow is shown in Ref. 8. Again, the agreement between predictions and experimental data is satisfying.

At sonic and low supersonic Mach numbers the blunt-nosed cylinder-flare bodies experience another type of flow separation, as illustrated in Fig. 5-16. The flow is attached at angles of attack below a certain critical value, α_d , but separates on the leeward side at higher α 's. Decreasing angle of attack gives reattaching of the leeward side flow, usually at a value below that causing separation. Even if one neglects this static aerodynamic hysteresis, the separation produces large nonlinear effects. The dynamic effects are again caused by time lag and mechanical phasing.

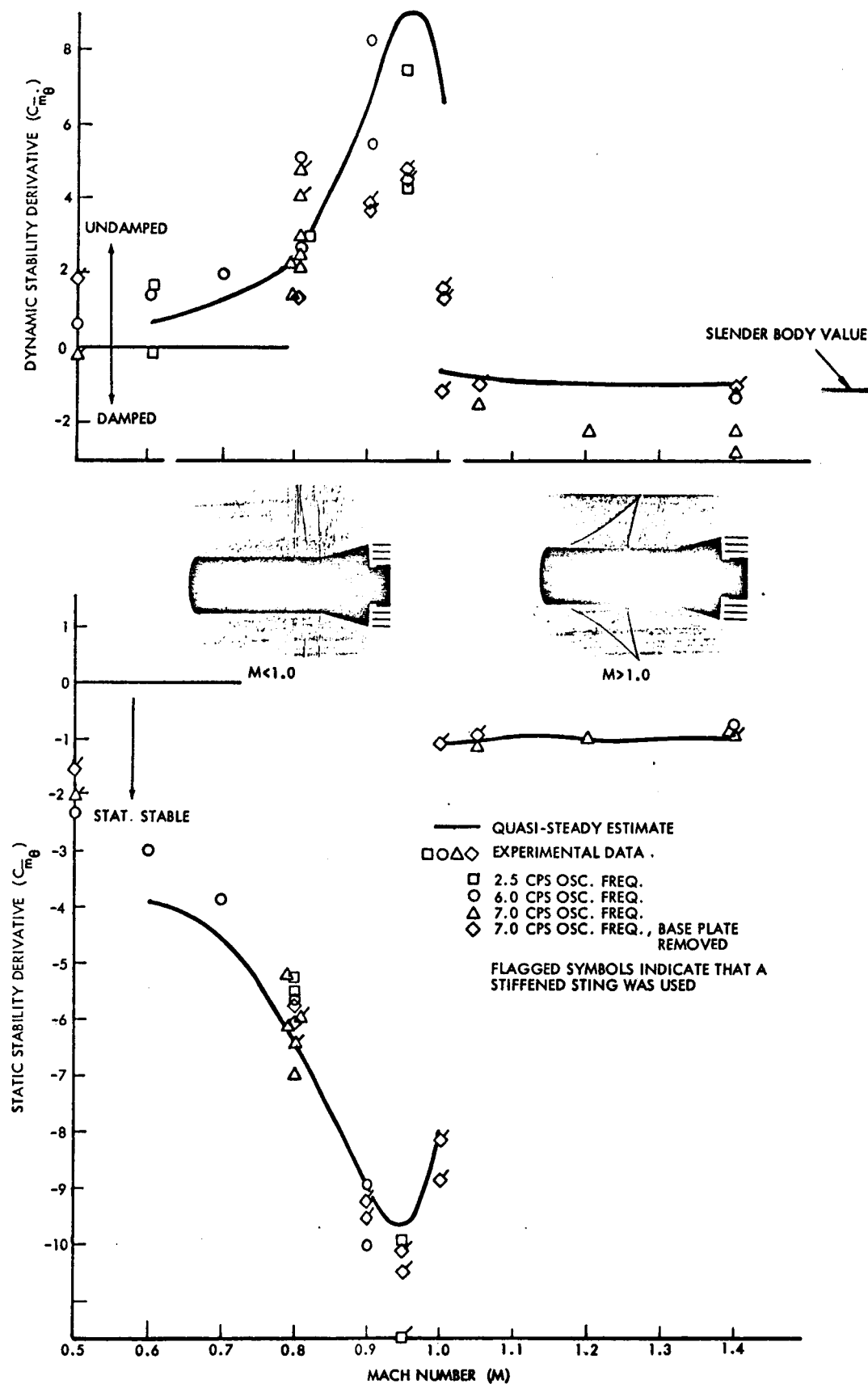


Fig. 5-14 Comparison Between Quasi-Steady Predictions and Measured Pitch Damping of a Blunt-Nosed Cylinder-Flare Body at Transonic Mach Numbers

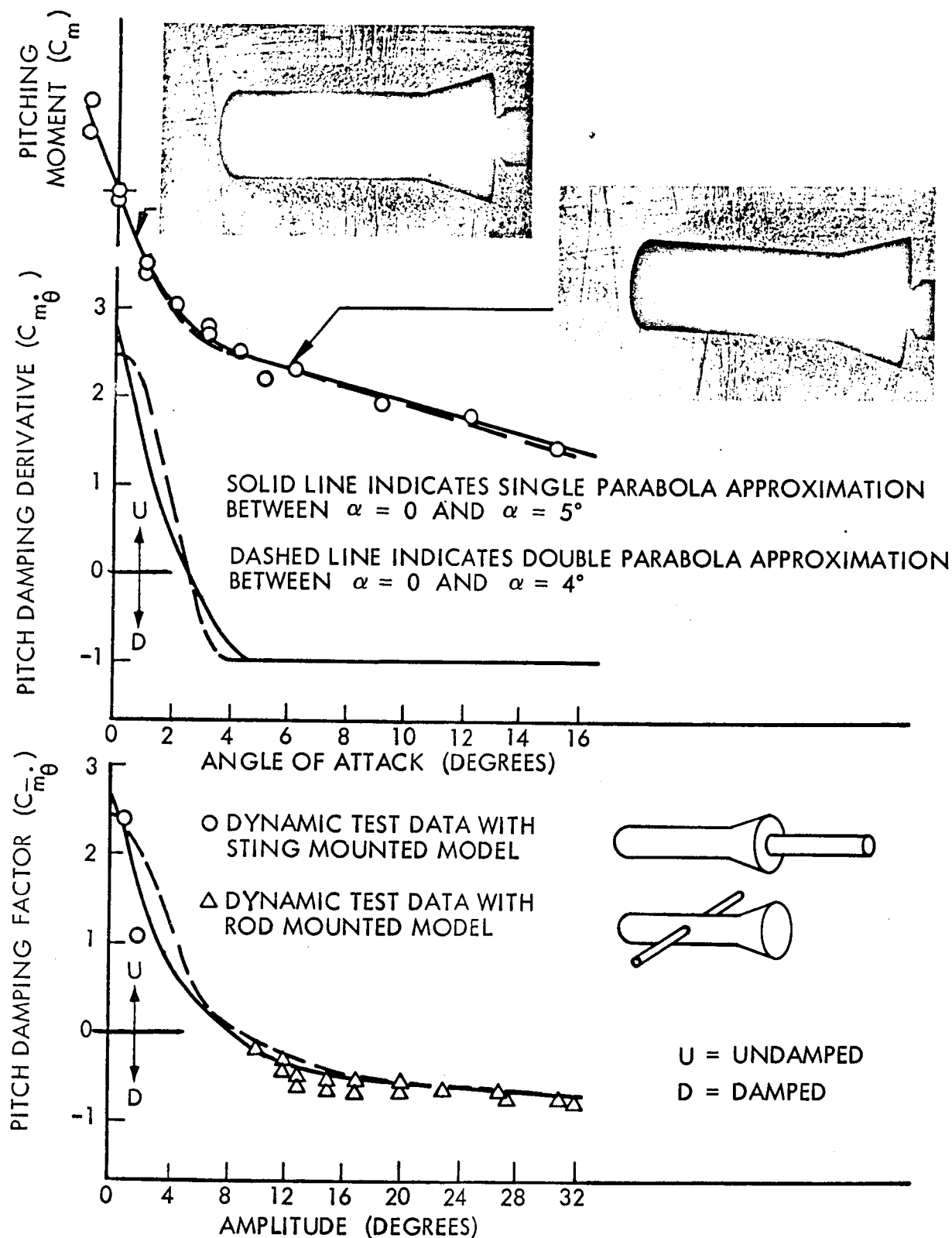


Fig. 5-15 Nonlinear Amplitude Effects Caused by Nose-Induced Separation

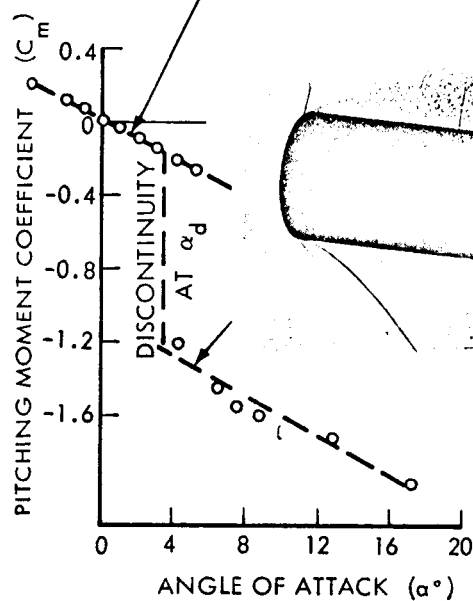
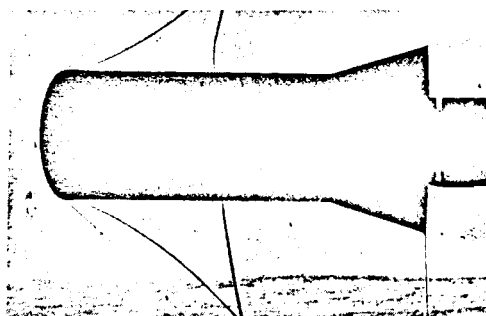
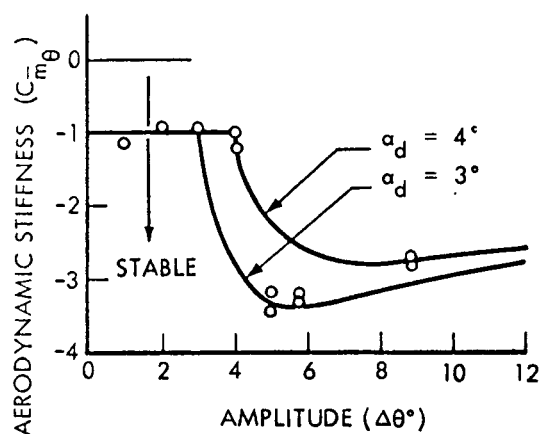
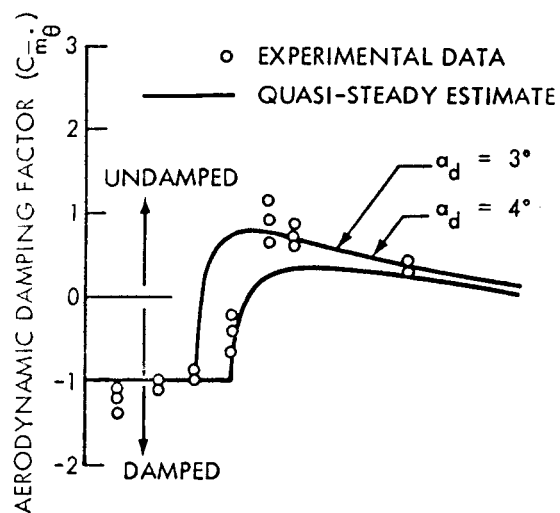


Fig. 5-16 Dynamic Effects of Separation-Induced Pitch Moment Discontinuity at Transonic Mach Numbers

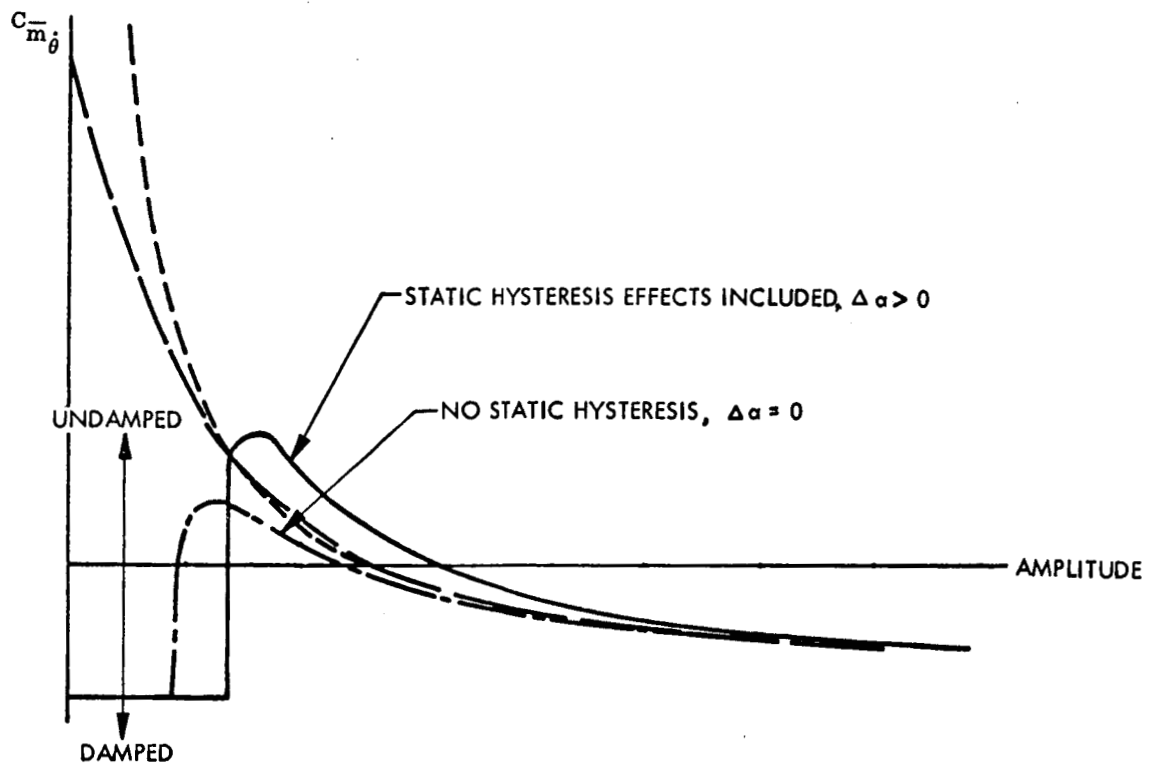
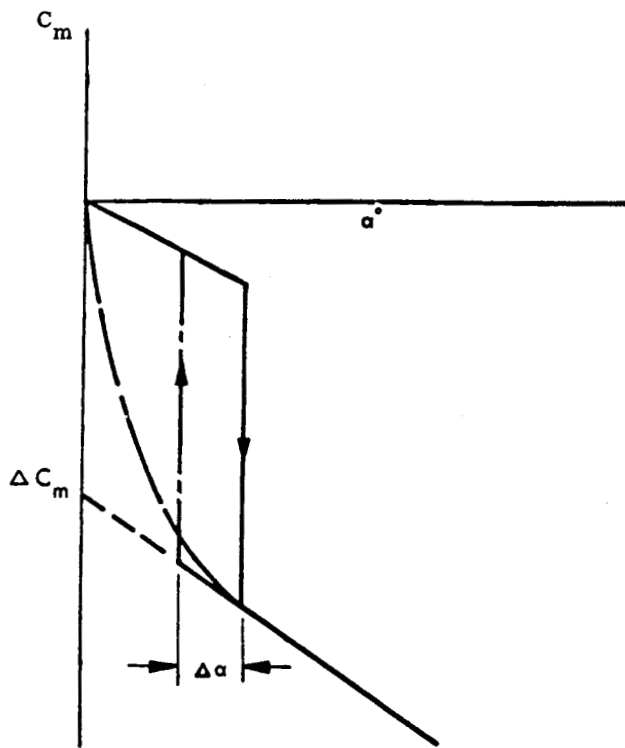
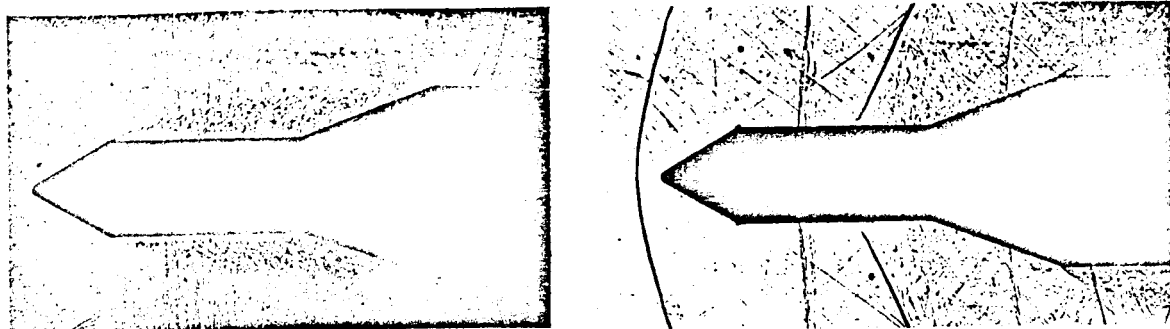
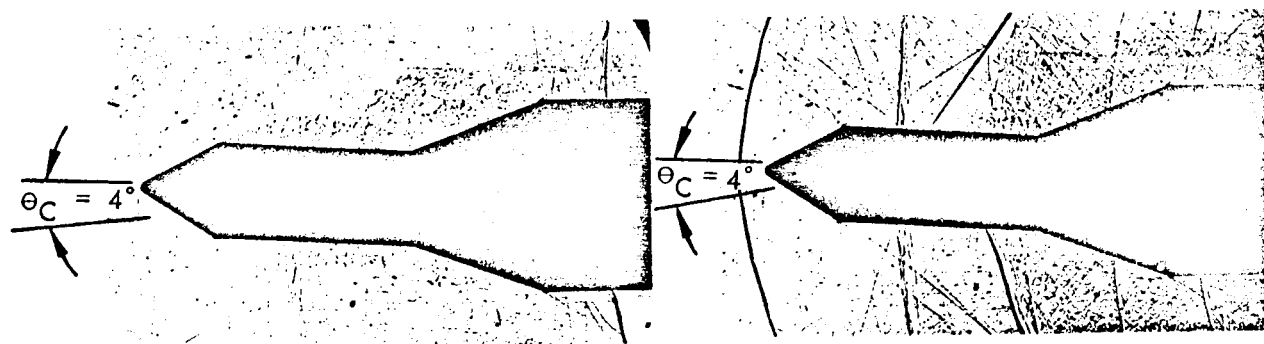
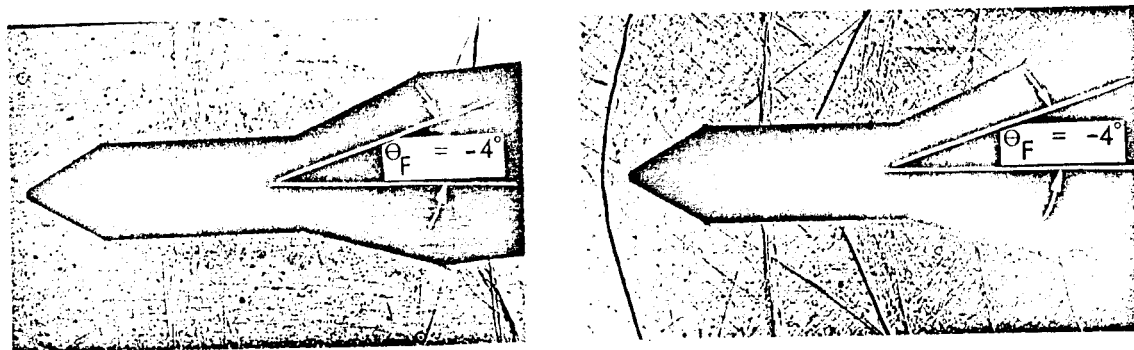


Fig. 5-17 Large Amplitude Pitch Damping

UNPERTURBED CASE AT $\alpha = 0^\circ$ 

CYLINDER ATTITUDE



FLARE ATTITUDE

A) NOSE-INDUCED
SEPARATION
 $M = .9$

B) SHOCK-INDUCED
SEPARATION
 $M = 1.2$

Fig. 5-18 Comparison Between Subsonic and Supersonic Separated Flow Patterns

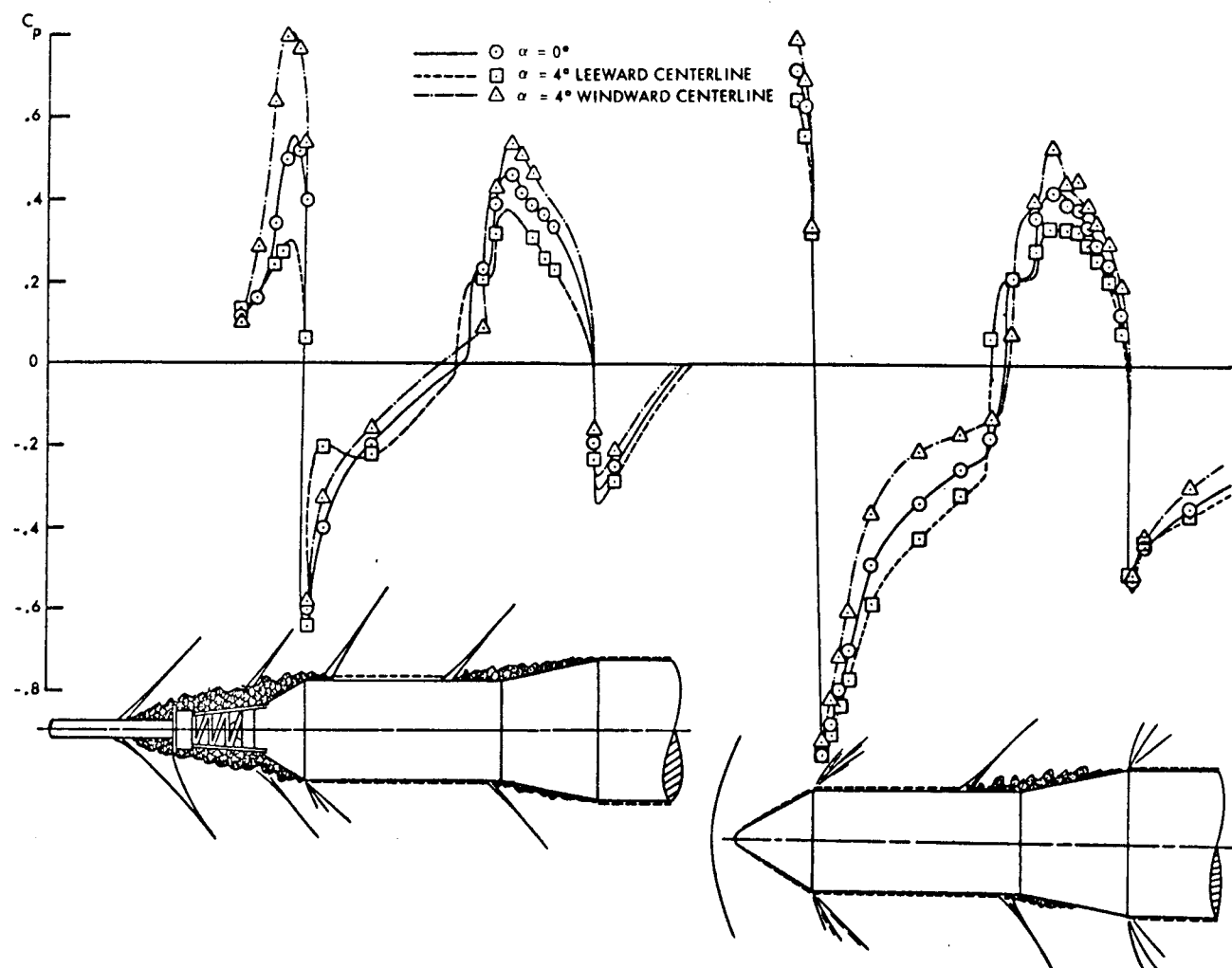


Fig. 5-19 Shock-Induced Separation Effects on the Saturn Forebody Pressure Distribution

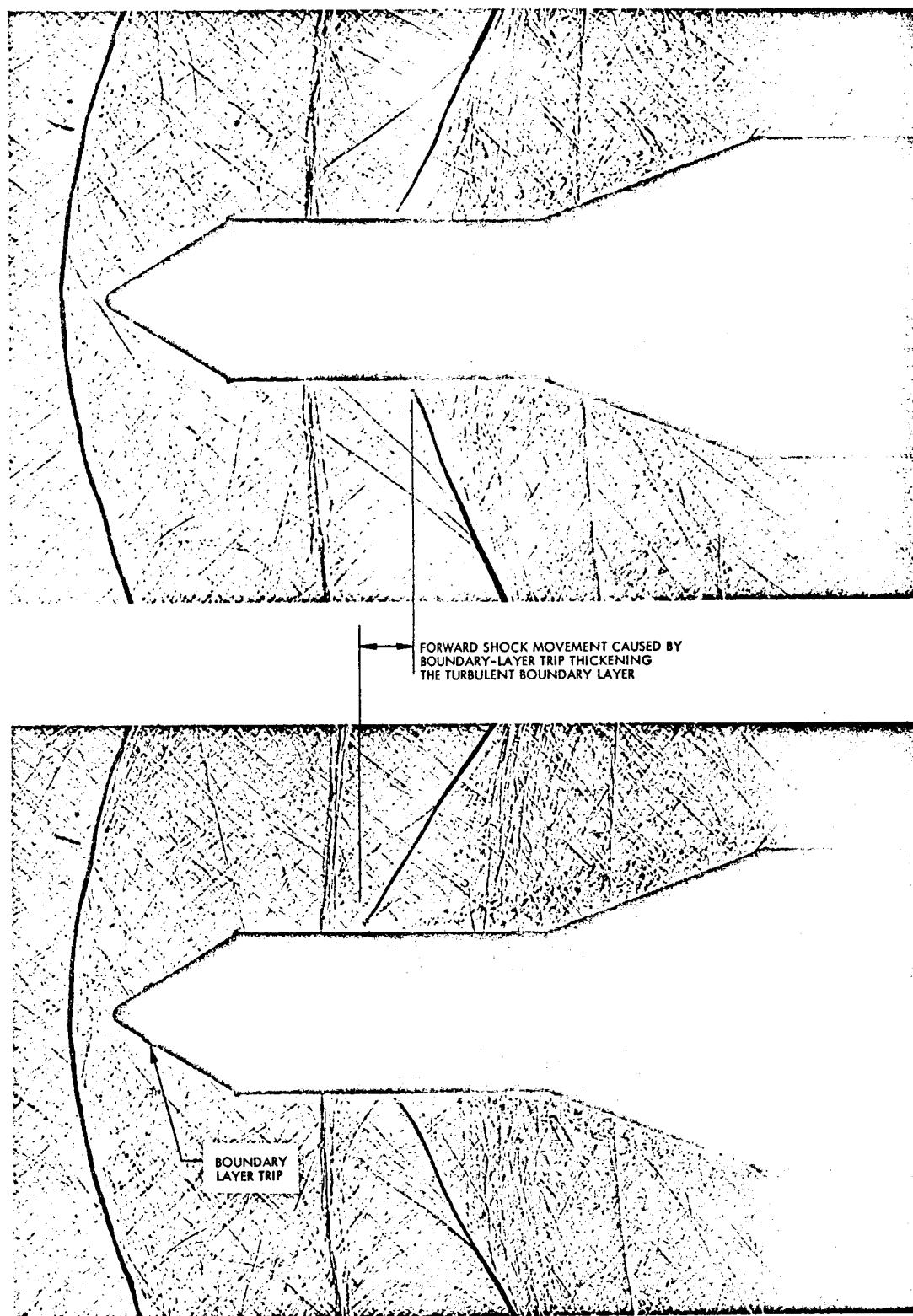


Fig. 5-20 Boundary Layer Thickness Effect on Shock-Induced Separation

The positive induced flare load is similar to that caused by the nose-induced separation, and the static and dynamic effects are also similar, although of lesser magnitudes. The negative shoulder load is a characteristic of all separated flow regions terminating aft of the shoulder. When the separated flow extent is decreased, the negative shoulder load decreases. This is also the case for the Apollo command module shoulder load generated by the escape rocket wake (Fig. 5-21). When the Mach number is increased, the wake contracts and the negative shoulder load is greatly reduced in magnitude. At the critical Saturn-Apollo service module length, an interaction between the reattaching escape rocket wake and the shock-induced separation occurs. The flare load suddenly increases where one would expect a minimum (Fig. 5-22). The peak flare load, correlatable with shock position, is due to a sudden increase in relative shock movement when the leeward shock moves forward on the reattaching separated flow while the windward shock moves aft on the reattached turbulent boundary layer.

The main phasing of the quasi-steady shock-induced load is generated by downstream time lag in realizing the effects of forebody crossflow. There are, however, secondary effects introduced through the upstream communication of changes in effective flare attitude as evidenced by the shadowgraphs in Fig. 5-18. These effects may not be too important except for certain critical flow geometries, such as the ones produced at critical tower lengths (Fig. 5-7) or critical cylinder lengths (Fig. 5-22). Fortunately, the overall effect of shock-induced separation is usually moderate, both statically and dynamically, due to the combination of positive and negative induced loadings (see Figs. 2-2 and 2-3).

The quasi-steady damping predictions for an elastic body compare well with what little experimental dynamic data that are available. At the NASA Langley Research Center, Rainey et al. have successfully undertaken the difficult task of simulating elastic vehicle dynamics in a wind tunnel test (Ref. 9). An 8-percent dynamically-scaled model of the Saturn I-Apollo vehicle was excited by an electromagnetic shaker in each of its first three bending modes, one at a time, and the aerodynamic damping was measured. The quasi-steady predictions agree, in general, with the measured damping for the three configurations tested (Figs. 5-23, 5-24, and 5-25). This is at least true for the first and second bending mode. The somewhat poor agreement for the third bending mode is probably attributable as much to the data sensitivity to the high modal

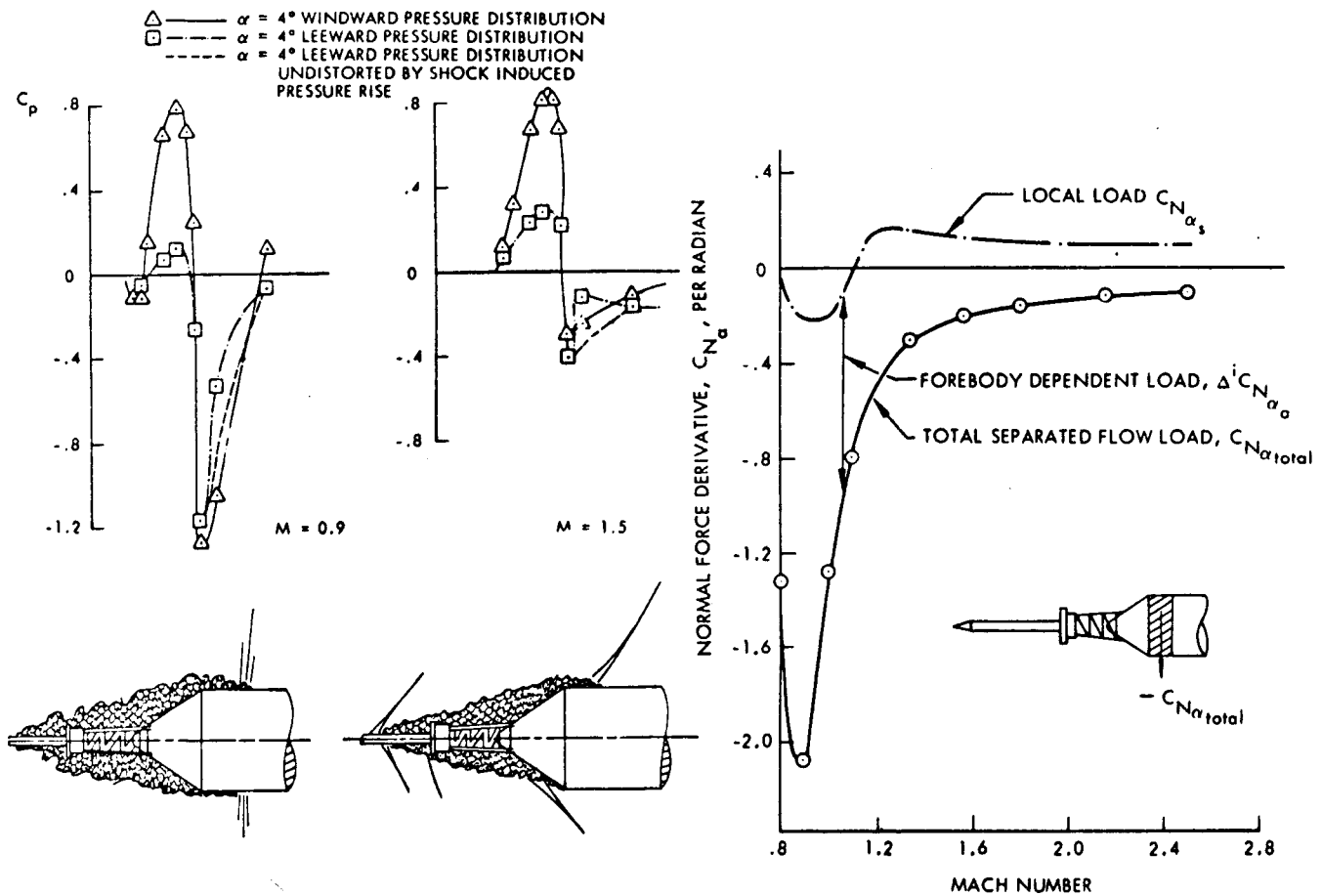


Fig. 5-21 Pressures and Loads on the Apollo Command Module Shoulder

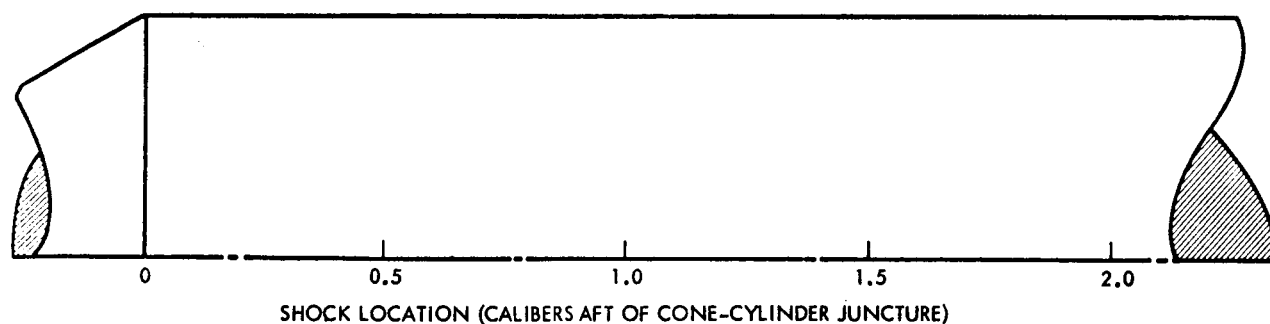
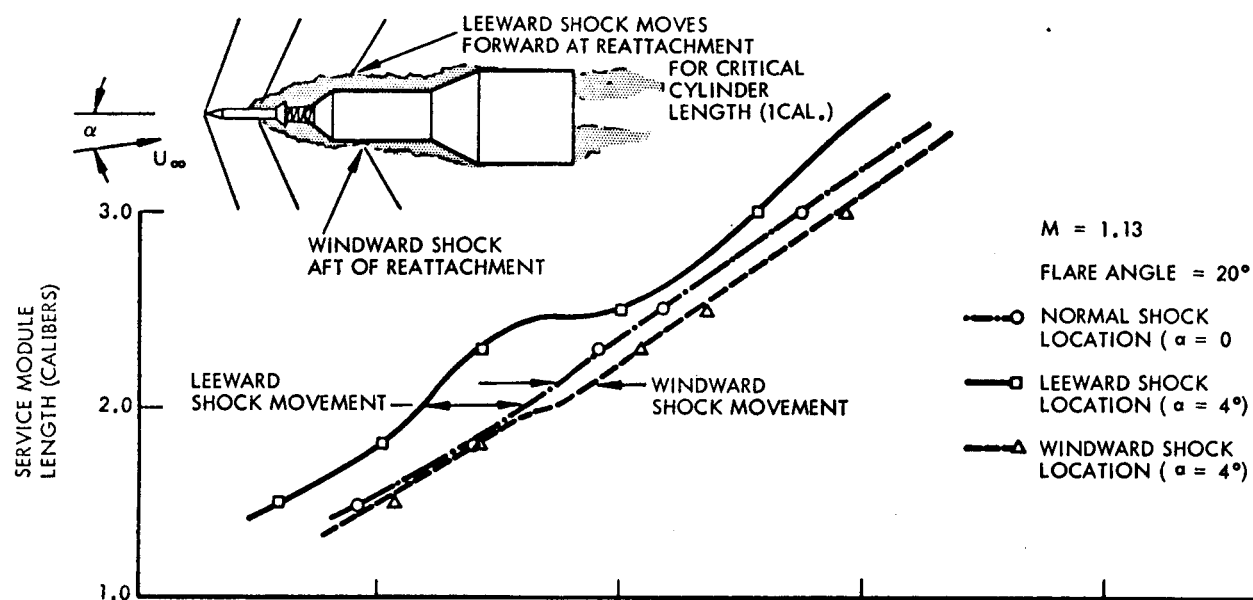
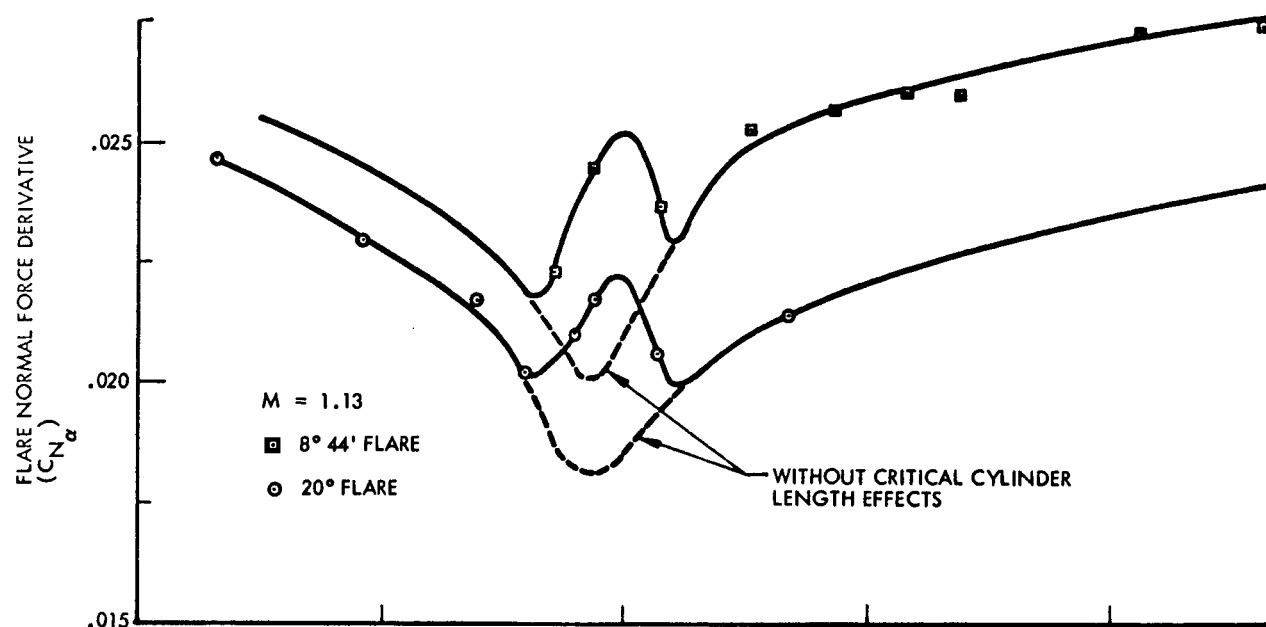


Fig. 5-22 Critical Cylinder Length Effects on the Saturn Forebody

deflections and slopes of the forebody as to the limitations of the quasi-steady method to predict damping for the third mode because of its higher reduced frequency.*

If the velocity deficit in the separated flow is neglected in computing the time lag, the separated flow effect on the damping is evidently underestimated (Fig. 5-23). Classic quasi-steady theory, which assumes the loads to be dependent upon local conditions only, as in the case of attached flow, obviously gives the wrong damping values (Fig. 5-23). This is especially true for the second bending mode, where the trend with Mach number becomes opposite to the trend of the experimental results. Increasing the downstream communication velocity to $U = U_{\infty}$ causes appreciable changes only in the first mode high Mach number damping. Even when the time lag effects are neglected, i.e., when $\bar{U} \rightarrow \infty$, the damping changes are large only for the first mode. It should be pointed out that some of the upstream dependence remains also for zero time lag (let $\bar{U} \rightarrow \infty$ in Eq. (5.14) of Ref. 4). On the whole, the agreement between measured and predicted damping is acceptable considering the scatter in the experimental data.**

At the NASA Ames Research Center, Cole, in his "partial mode" testing technique (Ref. 10), has dynamically simulated the forward portion of the Saturn I-Apollo configuration in its second bending mode. In Fig. 5-26, the quasi-steady prediction of the forebody damping for the second bending mode of the Langley configuration is shown for "disk on" and "disk off." The predictions agree generally with the trends measured by Cole. Both configurations are damped at subsonic speeds, whereas at supersonic speeds the disk gives a large undamping contribution. The reason for this is twofold. The primary cause is the loss of the slender body directing effect from the escape rocket, and the simultaneous increase in wake translation when the disk is mounted ahead of the escape rocket flare (See Section 4 and Fig. 4-3). The directing effect that is lost increases with Mach number in the transonic and low supersonic speed

*The pertinent characteristic length for the reduced frequency ($\omega d/U$) is the local cross-sectional diameter $d \leq D_{\text{ref}}$. For the third bending mode, $(\omega D_{\text{ref}}/U) \leq 0.75$ and the requirement for "quasi-steadiness," $(\omega d/U)^2 \ll 1$, is not satisfied over the whole vehicle.

**It should be pointed out that the total damping is the result of an ill-conditioned process of summing a number of positive and negative damping contributions (see Figs. 2-2 and 2-3). The large scatter in the experimentally measured damping (see Fig. 2-20) may be interpreted as evidencing the existence of the same problem when summing the contributions aerodynamically.

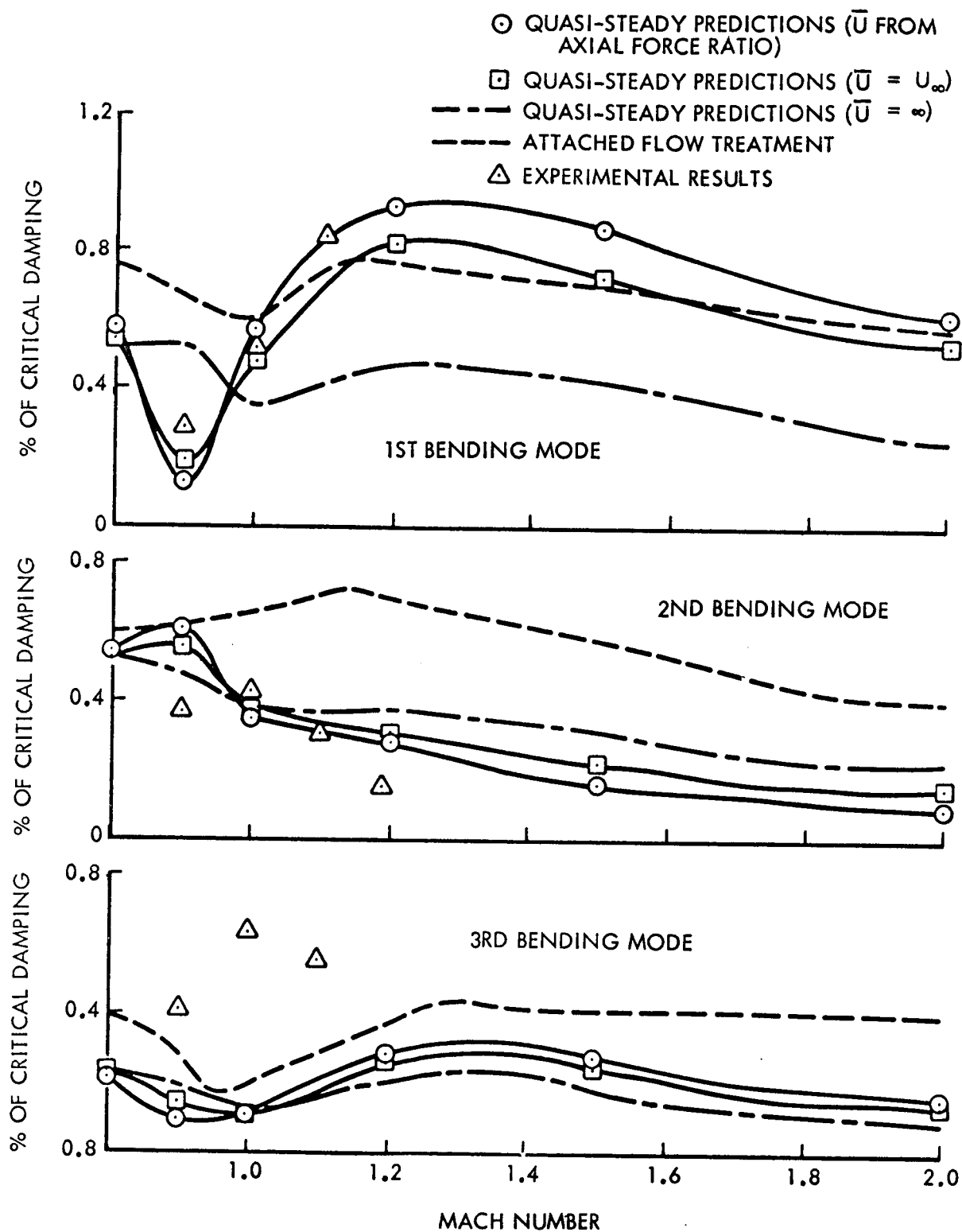


Fig. 5-23 Aerodynamic Damping at $\alpha = 0$ of the Saturn I-Apollo Launch Vehicle With Escape Rocket, Disk-On

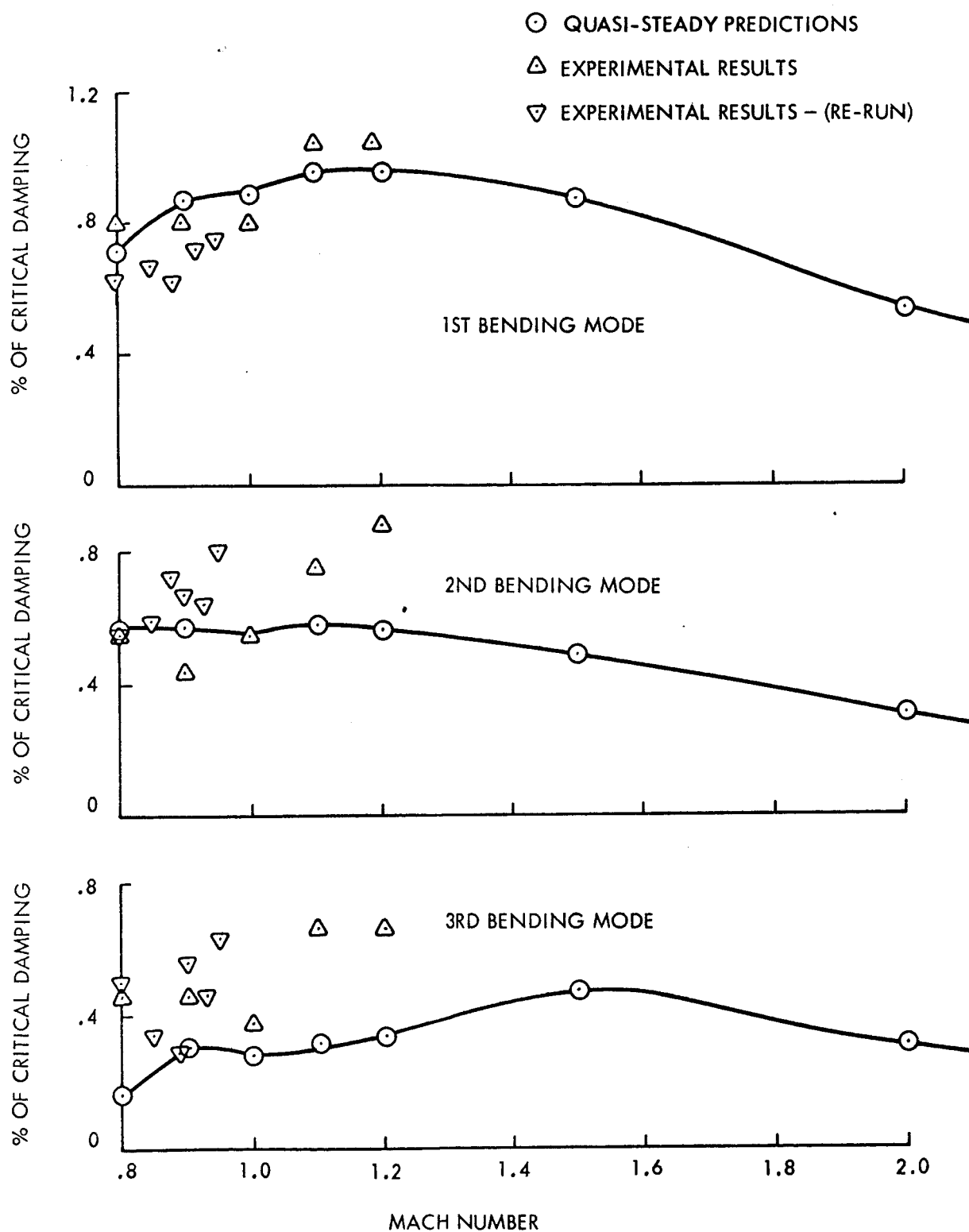


Fig. 5-24 Aerodynamic Damping at $\alpha = 0$ of the Saturn I-Apollo Launch Vehicle With Escape Rocket, Disk-Off

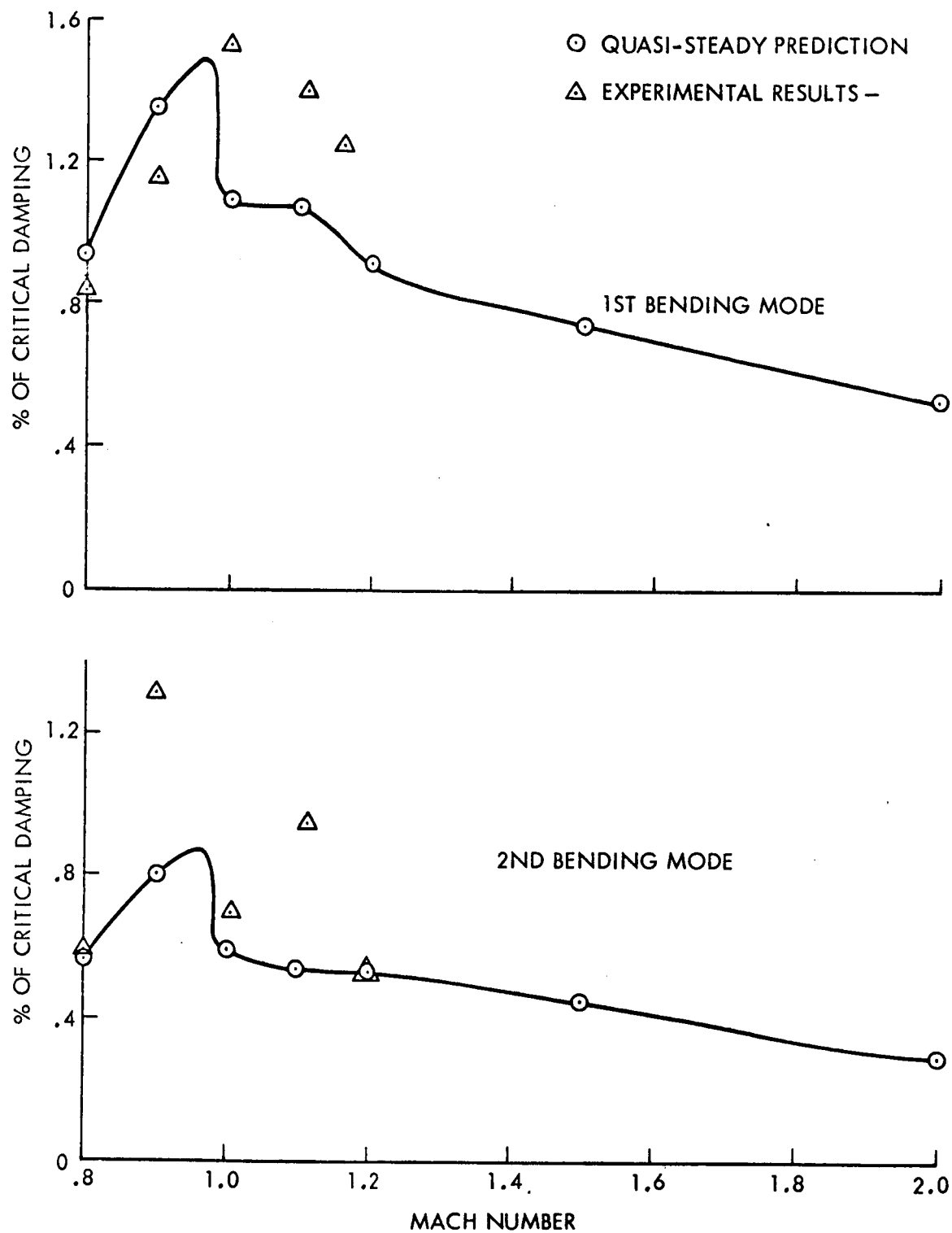


Fig. 5-25 Aerodynamic Damping at $\alpha = 0$ of the Saturn I-Apollo Vehicle Without Escape Rocket

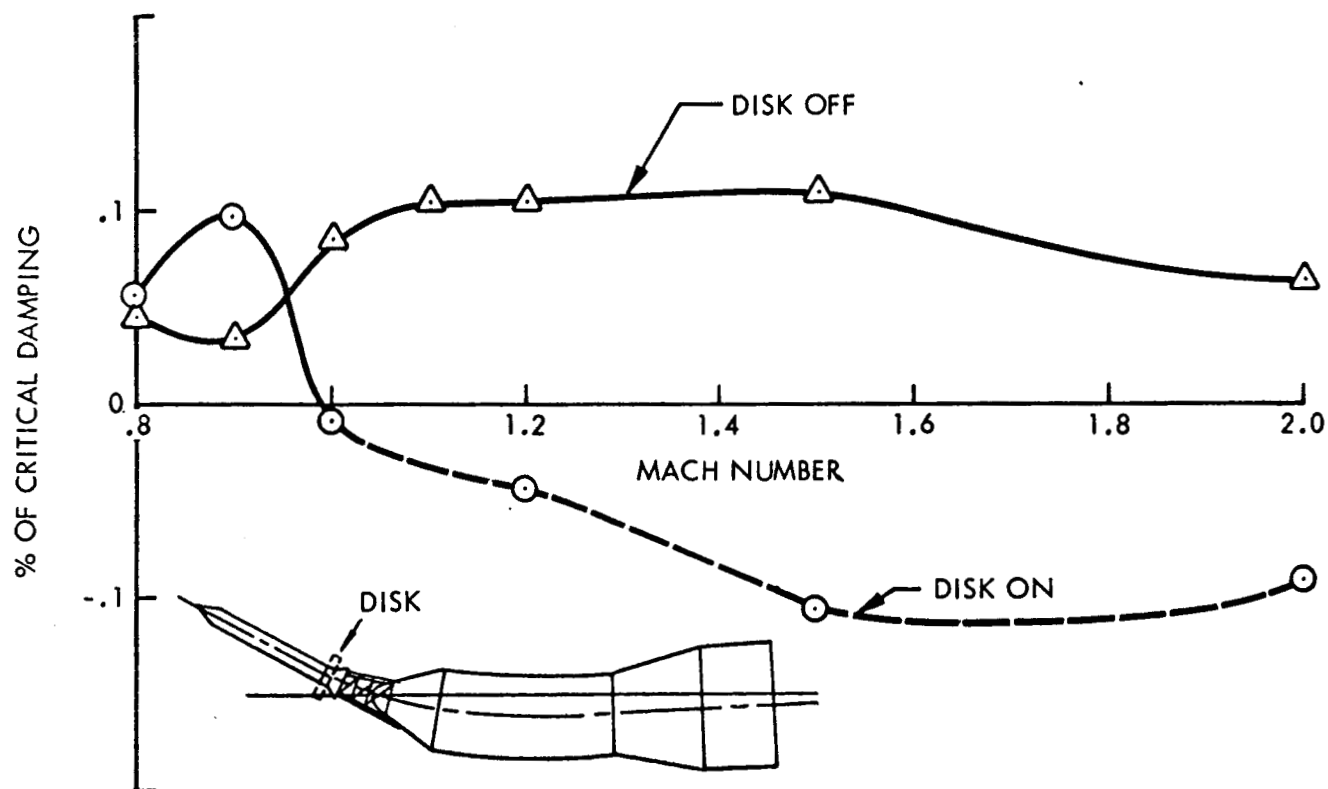


Fig. 5-26 Forebody Damping at $\alpha = 0$ for the Second Bending Mode of the Saturn-Apollo Launch Vehicle With Escape Rocket, Disk-On and Disk-Off.

regime. The secondary cause is the undamping axial force moment from the disk itself, which also increases with Mach number at moderate supersonic speeds, (see Figs. 5-5 and 5-6).

In Fig. 5-27 the computed forebody damping for the tower-off Saturn-Apollo configuration is shown for the second bending mode. When the loads aft of the flare are neglected, the results are comparable with the pitch damping measured on rigid bodies of similar geometry (see Fig. 5-13). Large subsonic undamping and moderate supersonic damping are typical for blunt-nosed cylinder-flare bodies. Furthermore, the allevating effect on the undamping of an added cylindrical skirt, which is caused mainly by the negative incremental shoulder load, is verified (Ref. 11) by observed trends in dynamic wind tunnel tests with rigid bodies (see Fig. 5-28).

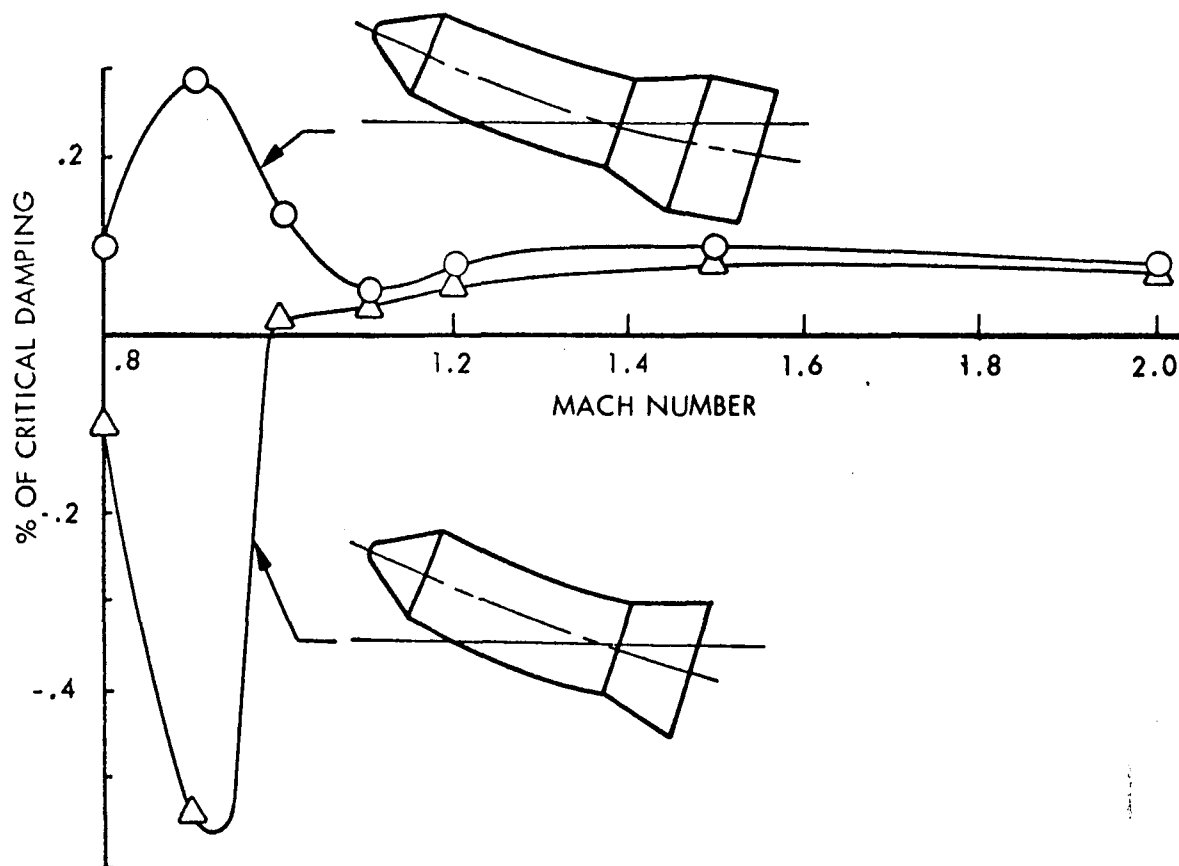


Fig. 5-27 Forebody Damping at $\alpha = 0$ for the Second Bending Mode of the Saturn-Apollo Launch Vehicle Without Escape Rocket

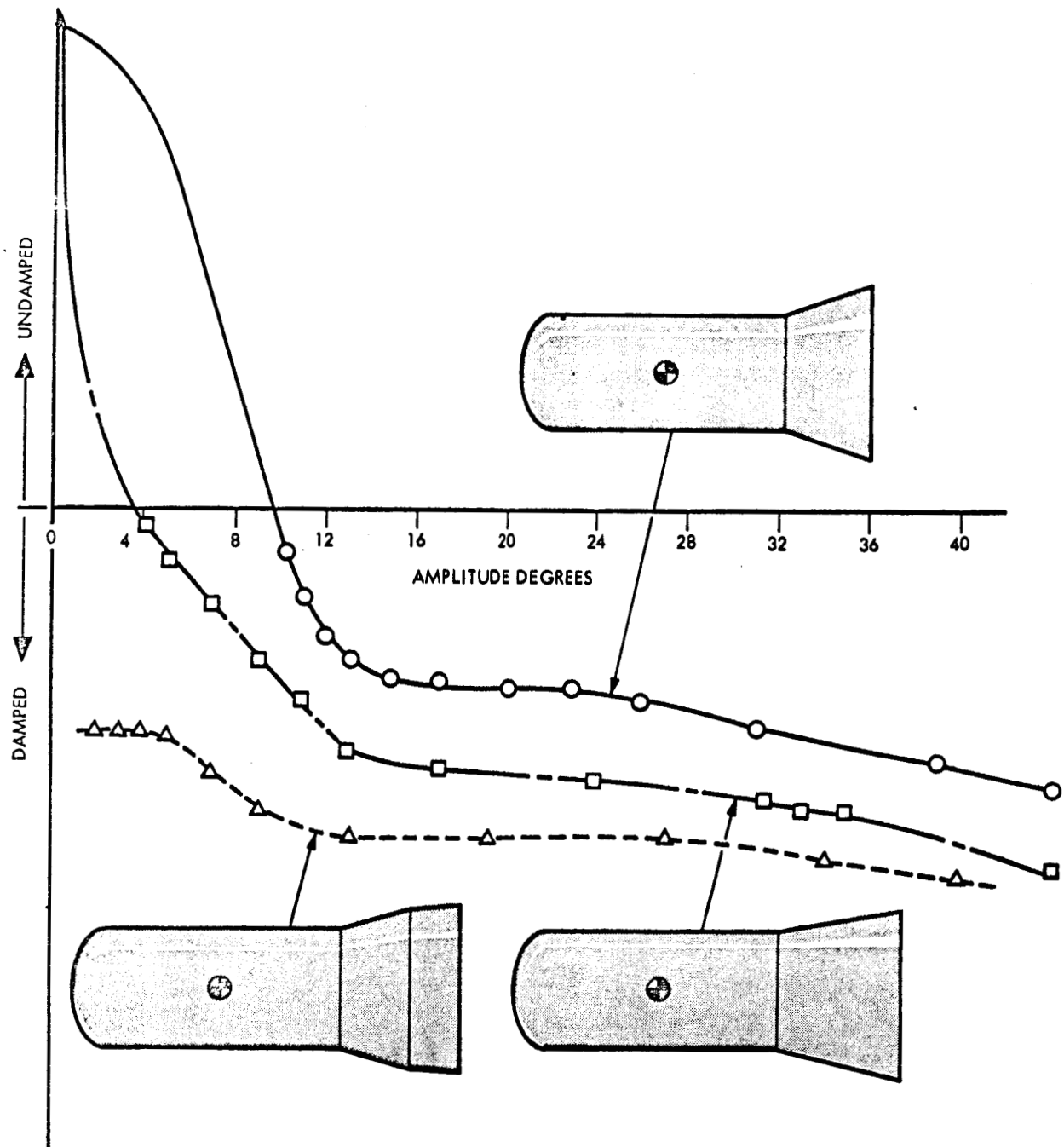


Fig. 5-28 Effect of Flare Geometry on Rigid Body Damping

Section 6

CONCLUSIONS

It has been shown that by using quasi-steady theory and experimental static data one may successfully compute the aerodynamic damping of a vehicle that is dominated by separated flow. The damping so computed has been shown to be in good agreement with experimental data in the transonic speed range. While the supersonic damping has been less well substantiated quantitatively, due to lack of experimental dynamic data, there appears to be substantial qualitative evidence supporting the predicted trends.

The results of the quasi-steady analysis reveal the following important dynamic characteristics of flow separation.

- Large regions of separated flow are capable of dominating both the static and dynamic characteristics of a vehicle in its rigid body mode as well as in its elastic body bending mode.
- The separated flow introduces finite time lag in the vehicle dynamics causing a sign reversal between static and dynamic effects. That is, the separation-induced force is statically stabilizing but dynamically destabilizing, and vice versa.
- The time lag effect is greatly amplified by mechanical phasing. Thus, moderate statically-stabilizing loads can cause drastically large undamping effects when a node or oscillation center is located between the separation source and the induced loading.

The quasi-steady method provides the designer with a powerful adjunct to dynamic testing. This approach not only provides a useful tool for predicting overall vehicle damping, but also, more important to the designer, it reveals the effect on the damping of each region of flow separation. Thus, problem areas may be pinpointed and eliminated early in the design phase without resorting to expensive and time-consuming "cut-and try" dynamic testing.

Section 7
REFERENCES

1. Lockheed Missiles & Space Company, "Steady Loads on Spiked Blunt Bodies of Revolution," by Lars-Eric Ericsson, LMSC TM 53-40-121 (LMSC-A312114), Contract NAS 8-5338, Sunnyvale, Calif., November 1962 (C)
2. Lockheed Missiles & Space Company, "Separated Flow Effects on the Static Stability of Cone-Cylinder-Flare Bodies," by J. Peter Reding, LMSC TM-53-40-119 (LMSC-802336), Contract NAS 8-5338, Sunnyvale, Calif., November 1962 (C)
3. Lockheed Missiles & Space Company, "Static Loads on the Saturn I-Apollo Launch Vehicle," by J. Peter Reding and Lars-Eric Ericsson, LMSC TM-53-40-143 (LMSC-803185), Contract NAS 8-5338, Sunnyvale, Calif., August 1963 (U)
4. Lockheed Missiles & Space Company, "Report on Saturn I-Apollo Unsteady Aerodynamics," by Lars-Eric Ericsson and J. Peter Reding, NAS 8-5338, Sunnyvale, Calif., February 1964 (U), *LMSC-A650215*
- (C) 5. Lockheed Missiles & Space Company, "Static Pressures and Forces Generated by a Flow Separation Disk," by Lars-Eric Ericsson, LMSC-804382, Contract NAS 8-5338, Sunnyvale, Calif., July 1964 (U)
- (dt) 6. Lockheed Missiles & Space Company, "Unsteady Characteristics of a Spiked Bluff Body," by Lars-Eric Ericsson, LMSC-804651, Contract NAS 8-5338, Sunnyvale, Calif., July 1964 (C)
7. Lockheed Missiles & Space Company, "Forces Induced on Bodies in Free Wakes and Three-Dimensional Cavities," by J. Peter Reding, LMSC-667990, Contract NAS 8-5338, Sunnyvale, Calif., December 1965 (U)
8. Lockheed Missiles & Space Company, "Separated Flow Effects on the Dynamic Stability of Blunt-Nosed Cylinder-Flare Bodies," by Lars-Eric Ericsson, LMSC-667991, Contract NAS 8-5338, Sunnyvale, Calif., December 1965 (C)

9. Rainey, G. , "Progress on the Launch Vehicle Buffeting Problem," 5th Annual Structures and Materials Conference of the American Institute of Aeronautics and Astronautics (AIAA, Palm Springs, Calif. , 1964), pp 163-177, (U)
10. NASA Ames Research Center, "Detection of Flow-Field Instability in the Presence of Buffeting by the Partial-Mode Model Technique," by H. A. Cole, Jr. , R. C. Robinson, and B. J. Gambucci, NASA TN D-2689, February 1965, (U).
11. U.S. Naval Ordnance Laboratory, White Oak, "Ballistic Missile Reentry Shapes," by I. Shantz and others, NAVORD Rept. 6066, Project NOL-363, White Oak, Maryland, 10 March 1958 (C)

Section 8

RECOMMENDATIONS FOR FUTURE STUDY

Obviously, the first recommendation for further study is an investigation of the dynamic effects of forward propagation within wakes and shock-induced separated flow regions. While the present Saturn vehicles appear to have avoided any significant such effects, future launch vehicles may not be so fortunate. It is suggested to measure experimentally the response of the submerged body to wake-source oscillations, and also measure local unsteady forces produced by the submerged body oscillation. In addition, the time history of the wake-source base pressure should be recorded while driving the submerged body. For shock-induced separation, where the same problem exists, the pressure fluctuation at the shock location in response to flare perturbations should be measured. These data would furnish direct measurements of both upstream and downstream time lags and their combined dynamic effects.

It is also desirable to improve the rigor of the partitioning of the negative shoulder load into local and induced components. Measurements of the fluctuating pressure in the shoulder region in response to wake source and submerged body oscillation would certainly enhance our knowledge about this phenomenon. This could be done in conjunction with the aforementioned time lag investigation. In addition, certain basic data are needed regarding the shock-induced separation, such as the rate of growth of the leeward boundary layer with angle of attack (and the corresponding windward side thinning). More detailed information about the submerged body loads could also be obtained as part of the investigation of the forward propagation time lag.

Finally, it is desirable to obtain further dynamic data for comparison with predictions. By varying frequency and spacing between wake source and submerged body, one can vary the perturbation wavelength to determine the limits of applicability of the quasi-steady technique. Again, such data may be obtained in conjunction with the forward time lag investigation.

The foregoing recommendations are aimed at achieving a degree of sophistication sufficient to allow application of the quasi-steady technique to an arbitrary launch configuration with a satisfactory degree of confidence. Continued efforts aimed at understanding the separation phenomena and their associated induced loads, and correlating all available experimental data with quasi-steady predictions, will contribute towards the ultimate goal of developing the capability of predicting vehicle static and dynamic characteristics by purely analytical means.

Appendix A

NOMENCLATURE

A	Axial force, kg, Coefficient $C_A = A/(\rho U^2/2) S$
c	Reference length, m, (usually $c = d$)
d	Body caliber, m
N	Normal force, kg, Coefficient $C_N = N/(\rho U^2/2) S$
L	Longitudinal distance, m
M	Mach number
M_A	Axial force pitching moment, kg-m, Coefficient $C_{m_A} = M_A/(\rho U^2/2) S c$
M_N	Normal force pitching moment, kg-m, Coefficient $C_{m_N} = M_N/(\rho U^2/2) S c$
p	Static pressure, kg/m^2
p_∞	Free stream static pressure, kg/m^2
q(t)	Normalized coordinate, m
q	Dynamic pressure, kg/m^2 , ($q = \rho U^2/2$)
q_∞	Free stream dynamic pressure, kg/m^2
$C_p = \frac{p - p_\infty}{q_\infty}$	Pressure coefficient
$S = \frac{\pi c^2}{4}$	Reference area, m^2
t, τ	Time, sec
U	Free stream velocity, m/s
\bar{U}	Mean convection velocity, m/s

x	Horizontal coordinate, m
$\xi = x/c$	Dimensionless x-coordinate
z	Vertical coordinate, m
α	Angle of attack, radians or degrees
β	Equivalent spike deflection angle, radians or degrees
Δ	Difference
ρ	Air density, $\text{kg-sec}^2/\text{m}^4$
ω	Free-free bending frequency, radians/sec
θ	Body attitude, radians or degrees
φ	Normalized modal deflection

Subscripts

a	attached flow
b	base
c	cylinder
F	generalized force
N	nose
Q.S.	Quasi-steady
s	separated flow
∞	undisturbed flow
0	At $\alpha = 0$

Superscripts

i induced e.g. $\Delta^i C_N$ = separation induced normal force
 ' induced by upstream communication, e.g. $C_{N_{\alpha'_s}}$

Differential Symbols

$$\varphi'(x) = \frac{\partial \varphi}{\partial x}$$

$$\dot{q}(t) = \frac{\partial q}{\partial t} ; \ddot{\theta}(t) = \frac{\partial^2 \theta}{\partial t^2}$$

$$C_{N_\alpha} = \frac{\partial C_N}{\partial \alpha} ; C_{m_\beta} = \frac{\partial C_m}{\partial \beta} ; C_{N_\theta} = \frac{\partial C_N}{\partial \theta}$$

Appendix B

REPORTS THAT HAVE SUPPLIED SUBSTANTIAL DATA INPUTS TO THE
STUDY OF DYNAMICS OF SEPARATED FLOW OVER BLUNT BODIES

- B.1 NASA, "Investigation of the Aerodynamic Characteristics of a Re-entry Capsule with Various Nose Shapes at a Mach Number of 2.91, Including Studies of Nose Spikes as a Means of Control," by R. W. Harman and W. B. Boatright, NASA TM X-426, January 1961 (C)
- B.2 -----, "Effect of Forebody Modifications on the Static Stability and Control Characteristics of a Re-entry Capsule at a Mach Number of 9.6," by W. O. Armstrong, NASA TM X-469, April 1961 (C)
- B.3 AFOSR, "Spiked Blunt Bodies in Supersonic Flow," by H. H. Album, AFOSR Report No. 307, June 1961 (U)
- B.4 NACA, "Initial Experiments on the Aerodynamic Cooling Associated with Large-Scale Vortical Motions in Supersonic Flow," by A. J. Eggers and C. A. Hermach, NACA RM A54L13, March 1955 (C)
- B.5 -----, "Flow Separation Ahead of Blunt Bodies at Supersonic Speeds," by W. E. Moeckel, NACA TN 2418, July 1951 (U)
- B.6 -----, "Flow Separation Ahead of a Blunt Axially Symmetric Body at Mach Numbers 1.76 to 2.10," by W. E. Moeckel, NACA RM E51I25, December 1951 (U)
- B.7 -----, "Heat Transfer from a Hemisphere-Cylinder with Flow Separation Spikes," by J. R. Stadler and H. V. Nielsen, NACA TN 3287, September 1951 (U)
- B.8 -----, "Investigation of the Flow Over a Spike-Nose Hemisphere-Cylinder at a Mach Number of 6.8," by D. H. Crawford, NASA TN D-118, December 1959 (U)

- B.9 S. M. Bogdonoff and I. E. Vas, "Preliminary Investigation of Spiked Bodies at Hypersonic Speeds," *Journal of Aerospace Sciences*, Vol 26, pp 65-74, February 1959 (U)
- B.10 NASA, "Laminar Heat Transfer and Pressure Distribution Studies on a Series of Re-entry Nose Shapes at a Mach Number of 19.4 in Helium," by R. D. Wagner, W. C. Pine, and A. Henderson, NASA TN D-891, June 1961 (U)
- B.11 D. J. Maull, "Hypersonic Flow Over Axially Symmetric Spiked Bodies," *Journal of Fluid Mechanics*, Vol 9, pp 584-592, August 1960 (U)
- B.12 NACA, "Reduction in Temperature-Recovery Factor Associated with Pulsating Flows Generated by Spike-Nose Cylinders at a Mach Number of 3.5," by C. A. Hermach, S. Krauss, and J. O. Reller, Jr. NACA RM A56L05, March 1957 (U)
- B.13 -----, "Flight Investigations at Supersonic Speeds to Determine the Effectiveness of Cones and a Wedge in Reducing the Drag of Round-Nose Bodies and Airfoils," by S. R. Alexander, NACA RM L58L07a, March 1959 (U)
- B.14 NASA, "Effects of Spike-Mounted Flow Deflectors on the Transonic Aerodynamic Characteristics of a Blunt-Nosed Body of Revolution Having a Cylindrical or Flared Afterbody," by S. L. Treon, R. M. Wakefield, and E. D. Knechtel, NASA TM X-574, October 1961 (C)
- B.15 NACA, "Flow Separation from Rods Ahead of Blunt Noses at Mach Number 2.72," by J. M. Jones, NACA RM L52E05a, July 1952 (U)
- B.16 BRL, "Effect on Drag of Two Stable Flow Configurations Over the Nose Spike of the 90 MM T316 Projectile," by B. G. Korpov and M. J. Piddington, BRL TN955, October 1954 (U)
- B.17 NACA, "Experimental Drag Coefficient of Round Noses With Conical Windshields at $M = 2.72$," by J. J. Jones, NACA RM L55E10, June 1955 (U)
- B.18 AEDC, "Aerodynamic Drag of Spiked Blunt Bodies in Low-Density Hypersonic Flow," by W. H. Sims and J. S. Hahn, AEDC TDR-64-160, August 1964 (U)

- B.19 NASA, "Effects of Nose-Cone Angle on the Transonic Aerodynamic Characteristics of a Blunt Cone-Cylinder Body Having a Cylindrical, Flared, or Blunt-Finned Afterbody," by S. L. Treon, NASA TM X-582, October 1961 (C)
- B.20 AEDC, "Influence of Several Shape Parameters on the Aerodynamics of Ballistic Re-entry Configuration," by J. E. Rittenhouse and H. Kaupp, Jr., AEDC-TR-60-13, December 1960 (C)
- B.21 NASA, "Transonic Static Aerodynamic Characteristics of a Blunt Cone-Cylinder Body with Flared Afterbodies of Various Angles and Base Areas," by R. M. Wakefield, E. D. Knechtel and S. L. Treon, NASA TM X-106, December 1959 (C)
- B.22 -----, "Effects of Centerbody Length and Nose Shape on the Transonic Characteristics of Low-Fineness-Ratio Bodies of Revolution with a Flared Afterbody," by R. M. Wakefield, S. L. Treon, and E. D. Knechtel, NASA TM X-366, May 1960 (C)
- B.23 -----, "The Effect of Nose Shape on the Static Aerodynamic Characteristics of Ballistic-Type Missile Models at Mach Numbers from 0.6 to 1.4," by S. L. Treon, NASA Memo 5-18-59A, May 1959 (C)
- B.24 -----, "Transonic Static Aerodynamic Characteristics of a Blunt Cone-Cylinder Body with Flared Afterbody and Blunt Cruciform Fins," by E. D. Knechtel, S. L. Treon, and R. M. Wakefield, NASA TM X-40, August 1959 (C)
- B.25 -----, "Comparison of the Effectiveness of Flares with that of Fins for Stabilizing Low-Fineness-Ratio Bodies at Mach Numbers from 0.6 to 5.8," by L. H. Jorgensen, J. R. Spahn, and W. A. Hill, Jr., NASA TM X-653, May 1962 (C)
- B.26 AEDC, "Static Stability Characteristics of a Flat-Nosed Cylinder with an Extensible Flare at Mach Numbers from 0.6 through 1.5," by L. E. Rittenhouse, AEDC-TDR-62-21, February 1962 (C)
- B.27 NASA, "Flare Separation of Ellipsoidal-Nosed Cylinder-Flare Models at Transonic Mach Numbers," by J. W. Cleary, NASA TM X-506, May 1961 (C)

- B.28 -----, "Effect of Nose Shape and Afterbody Flare on the Transonic Characteristics of a Low-Fineness-Ratio Body of Revolution," by S. L. Treon, R. M. Wakefield, and E. D. Knechtel, NASA TM X-164, March 1960 (C)
- B.29 -----, "Transonic Static Aerodynamic Characteristics of a Low-Fineness-Ratio Body of Revolution Having a Blunt Ellipsoidal Nose and Flare Afterbodies of Various Angles and Base Areas," by E. D. Knechtel, R. M. Wakefield, and S. L. Treon, NASA TM X-113, January 1960 (C)
- B.30 -----, "Some Effects of Nose Bluntness and Fineness Ratio on the Static Longitudinal Aerodynamic Characteristics of Bodies of Revolution at Subsonic Speeds," by W. C. Hayes, Jr., and W. P. Henderson, NASA TN D-650, February 1961 (U)
- B.31 -----, "An Investigation of the Static and Dynamic Aerodynamic Characteristics of a Series of Blunt-Nosed Cylinder-Flare Models at Mach Numbers from 0.65 to 2.20," by D. E. Reese, Jr., and W. R. Wehrend, Jr., NASA TM X-110, January 1960 (C)
- B.32 -----, "The Effects of Nose Bluntness on the Flare Separation and Longitudinal Characteristics of Ellipsoidal-Nosed Cylinder-Flare Models at Transonic Speeds," by J. W. Cleary, NASA TM X-370, July 1960 (C)
- B.33 -----, "Turbulent Boundary-Layer Separation Induced by Flares on Cylinders at Zero Angle of Attack," by D. M. Kuehn, NASA TR R-117, 1961 (C)
- B.34 NACA, "The Effects of Boundary-Layer Separation over Bodies of Revolution with Conical Tail Flares," by D. Dennis, NACA RM A57I30, December 1957 (U)
- B.35 AEDC, "Boundary Layer Separation Effects on the Static Stability of a Flare-Tail Missile Configuration at $M = 2$ to 6," by J. D. Gray, AEDC-TN-60-103, June 1960 (U)
- B.36 RAE, Gr. Britain, "A Simplified Model of Incompressible Flow Past Two-Dimensional Airfoils with a Long Bubble Type of Flow Separation," by J. F. Norbury and L. F. Crabtree, RAE TN Aero 2352, June 1955 (U)

- B.37 R. J. Vidal, "The Influence of Two-Dimensional Stream Shear on Airfoil Maximum Lift," ARS Paper No. 61-120-1814, June 1961 (U)
- B.38 NASA, "Aerodynamic Characteristics of Spherically Blunted Cones at Mach Numbers from 0.5 to 5.0," by R. V. Owens, MSFC Report No. MTP Aero-61-38, May 1962 (U)
- B.39 NACA, "Effect of a Discontinuity on Turbulent Boundary Layer-Thickness Parameters with Application to Shock-Induced Separation," by E. Reshotko and M. Tucker, NACA TN 3454, May 1955 (U)
- B.40 -----, "Pressure Rise Associated with Shock-Induced Boundary-Layer Separation," by E. S. Love, NACA TN 3601, October 1955 (U)
- B.41 -----, "Investigation of Separated Flow in Supersonic and Subsonic Streams with Emphasis on the Effect of Transition," by D. R. Chapman, D. M. Kuehn, and H. K. Larson, NACA TR 1356 (also TN 3869), March 1957 (U)
- B.42 University of London, "A Study of Hypersonic Separated Flows," by C. J. Wood, PhD-Thesis, ASTIA AD-401652, October 1961 (U)
- B.43 BRL, "The Transition from a Turbulent to a Laminar Boundary Layer," by J. Sternberg, BRL906, May 1954 (U)
- B.44 S. F. Horner, "Fluid Dynamic Drag," 1958 (U)
- B.45 NASA, "Results of a Wind Tunnel Investigation to Determine Pressure and Load Distribution over the Saturn C-1, Block II Vehicle," by J. O. Windman and A. C. Seiber, MSFC Memo No. M-Aero-E-110-62, September 1962 (U)
- B.46 Cornell Aeronautical Laboratory, "Transonic Wind Tunnel Tests of a .0175 Scale Pressure Model of the Saturn C-1, Block II Launch Vehicle," by D. L. Millikan, Report No. HM-15-10-V-8, July 1963
- B.47 North American Aviation, "Stability and Control Manual," by D. C. Olsen, NAA ATS/60-159, 1960 (U)

- B.48 NASA, "A Second-Order Shock-Expansion Method Applicable to Bodies of Revolution Near Zero Lift," by C. A. Syvertson and D. H. Dennis, NACA TR 1328, 1957 (U)
- B.49 ARGMA, "Comparison of Second-Order Shock-Expansion Theory with Data for Cone-Cylinder-Frustum Bodies of Revolution at Supersonic Mach Numbers," by J. C. Craft, ARGMA TN/GGN, 31 December 1959 (C)
- B.50 NACA, "Zero Lift Drag of Several Conical and Blunt Nose Shapes Obtained in Free Flight at Mach Numbers of .7 to 1.3," by R. O. Pitland and L. W. Putland, NACA RM L54A23, March 23, 1954 (U)
- B.51 NACA, "Results of Tests to Determine the Effect of a Conical Windshield on the Drag of a Bluff Body at Supersonic Speeds," by S. R. Alexander, NACA RM L56K08a, January 1947 (U)
- B.52 Preliminary Unpublished Static Pressure Distribution Data on a 5.5 Percent Saturn-Apollo Model (PSTL-1), Obtained from the Experimental Aerodynamics Branch, Aeroballistics Division, George C. Marshall Space Flight Center (U)
- B.53 R. V. Dogget, Jr., and P. W. Hanson, "Preliminary Results of the Saturn-Apollo 5 Percent Scale Aeroelastic Model Studies," Minutes of Aeroelastic and Acoustic Conference, Houston, NASA Manned Spacecraft Center, 6 March 1963 (C)
- B.54 H. Cole, Jr., "Dynamic Response of the Apollo Partial - Mode Model at Subsonic and Supersonic Mach Numbers," Minutes of Aeroelastic and Acoustic Conference, Houston, NASA Manned Spacecraft Center, 6 March 1963 (C)
- B.55 Jet Propulsion Laboratory, "The Fluctuating Pressure Field in a Supersonic Turbulent Boundary Layer," by A. L. Kistler and W. S. Chan, TR 32-277, Pasadena, California, August 1962 (U)
- B.56 NASA Langley Research Center, "Transmittal of Preliminary Data Concerning Aerodynamic Damping, Determined Experimentally from the 8 Percent Apollo/Saturn Aeroelastic Model SD-1," Langley Field, Va., 4 April 1963 (C)

- B. 57 U.S. Naval Ordnance Laboratory, "Ballistic Missile Re-Entry Shapes," by I. Shantz et. al., NAVORD Rept 6066, 10 March 1958
- B. 58 North American Aviation, "Preliminary Data From FS-2 Component Loads Model Tests in NASA-Ames Unitary Plan Wind Tunnels," Sep 1962 (C)
- B. 59 R. L. Bisplinghoff, H. Ashley, and R. L. Halfman, Aeroelasticity, Cambridge, Mass., Addison-Wesley, 1955 (U)
- B. 60 NASA, "Preliminary Vibration Analysis of SA-6," by L. Kiefling, MSFC Memo, M-AERO-D-876-8222, 20 May 1963 (U)
- B. 61 -----, "Two-Stage Saturn I Orbital Trajectory (SAG)," MSFC Memo, M-AERO-TT-863, Mar 1963 (C)
- B. 62 NACA, "Equations, Tables, and Charts for Compressible Flow," Ames Research Staff, NACA Report R-1138, 1953
- B. 63 Brown Engineering, "Basic Data Release of Investigation to Determine The Dependence of Afterbody Loads on Forebody Attitude for Tower Mounted Wake Sources," by W. C. Pope, Jr., TM AA-7-64-2, 21 July 1964 (U)
- B. 64 -----, "Basic Data Release of Phase II of Investigation to Determine The Dependence of Afterbody Loads on Forebody Attitude for Tower Mounted Wake Sources," by W. C. Pope, Jr., TM AA-1-65-4, 20 Jan 1965 (U)
- B. 65 NASA "Aerodynamic Characteristics of Towed Cones Used as Decelerations at Mach Numbers from 1.57 to 4.65," by N. Charczenko and J. T. McShera, NASA TN D-994, Dec 1961 (U)
- B. 66 Air Force Flight Dynamics Laboratory, "Drag Characteristics of Several Two-Body Systems at Transonic and Supersonic Speeds," by H. G. Heinrich and S. Hess, RTD-TDR-63-4226, Dec 1964 (U)
- B. 67 AEDC, "Static and Dynamic Testing of Conical Trailing Decelerators for the Pershing Re-Entry Vehicle," by J. D. Coats, AEDC-TN-60-188, Oct 1960 (U)
- B. 68 AEDC, "An Investigation of the Influence of Several Shape Parameters on the Aerodynamics of Ballistic Re-Entry Configurations, Phase I, Mach Numbers 0.70 through 1.40," by L. E. Rittenhause and H. Kaupp, Jr., AEDC-TN-59-16, May 1959 (U)

- B. 69 NASA, "Effect of Nose Shape and Afterbody Flare on the Transonic Characteristics of a Low-Fineness-Ratio Body of Revolution," by S. L. Treon, R. M. Wakefield, and E. D. Knechtel, NASA TM X-164, March 1960 (C)
- B. 70 -----, "Free-Flight Investigation of a Flare-Stabilized Blunt Nose Reentry Body Having a Fineness Ratio of 3.11 at Mach Numbers From 0.7 to 1.90, (U)," by R. J. Mayhue and W. S. Blanchard, Jr., NASA TM X-214, March 1960 (C)
- B. 71 AEDC, "Wind Tunnel Tests to Determine the Static Stability of Two Polaris Re-Entry Configurations at Transonic Speeds," by H. Kaupp and L. E. Rittenhouse, AEDC TN 60-95, June 1960 (C)
- B. 72 -----, "Wind Tunnel Measurements of Forces and Pressures on Three 0.7-Scale Polaris Re-Entry Configurations," by J. H. Nichols and B. H. Johnson, AEDC-TN-60-102, June 1960 (C)
- B. 73 NASA, "Free-Flight Measurements of the Base Pressures and Drag of a Flare-Stabilized Cylindrical Reentry Body with an Elliptical Blunt Nose at Mach Numbers from 1.9 to 0.7," by R. J. Mayhue, NASA TM X-309, September 1960 (C)
- B. 74 -----, "The Effect of Air Bleed on the Heat Transfer and Pressure Distribution on 30° Conical Flares at a Mach Number of 6.8," by D. H. Crawford, NASA TM X-439, March 1961 (U)
- B. 75 AEDC, "Results of Force and Pressure Tests on Several Blunt Lifting Bodies at Mach Numbers 1.5, 3, 6, and 8," by W. T. Strike, J. Jones, and J. Myers, AEDC-TN-61-39, April 1961 (U)
- B. 76 NASA, "Heat Transfer and Pressure Distribution at a Mach Number of 6.8 on Bodies with Conical Flares and Extensive Flow Separation," by J. V. Becker and P. F. Korycinski, NASA TN D-1260, April 1962 (U)
- B. 77 AEDC, "Force Tests of Standard Hypervelocity Ballistic Models HB-1 and HB-2 at Mach 1.5 to 10," by J. D. Gray and E. E. Lindsay, AEDC TDR 63-137, August 1963 (U)

- B. 78 NASA, "Static Longitudinal Stability and Axial Force Characteristics of a 4.33-Caliber Blunt Cylinder with a 30° Slotted Frustum Afterbody over a Mach Number Range of 0.50 to 4.96," by R. E. Pitcock, NASA TM X-53283, June 1965 (U)
- B. 79 NACA, "Stability Investigation of a Blunt Cone and a Blunt Cylinder with a Square Base at Mach Numbers from 0.64 to 2.14," by L. C. Coltrane, NACA RM L58G24, September 1957 (U)
- B. 80 -----, "Stability of Ballistic Re-Entry Bodies," by J. D. Bird and D. E. Reese, Jr., NACA RM L58EO2a, August 1958 (C)
- B. 81 NASA, "Damping in Pitch and Static Stability of a Group of Blunt-Nose and Cone-Cylinder-Flare Models at a Mach Number of 6.83," by H. S. Fletcher and W. D. Wolhart, NASA Memo 5-6-59L, May 1959 (C)
- B. 82 AEDC, "An Investigation of the Influence of Reynolds Number on the Dynamic Stability of Three Ballistic Re-Entry Configurations at Transonic Speeds," by J. A. Black and R. C. Bauer, AEDC-TN-60-44, March 1960 (U)
- B. 83 NASA, "The Transonic Damping in Pitch of Three Cylinder-Flare Models with Various Degrees of Nose Bluntness," by H. F. Emerson and R. C. Robinson, NASA TM X-368, August 1960 (C)
- B. 84 BRL, "Free-Flight Aerodynamic Data of Four AVCO Advanced Design Configurations," by E. D. Boyer, BRL MR 1296, August 1960 (C)
- B. 85 L. E. Rittenhouse, "Comments on the Aerodynamics of the Cone-Cylinder-Flare Ballistic Reentry Shape," Fifth Symposium on Ballistic Missile and Space Technology, Los Angeles, 24-31 August, 1960 (C)
- B. 86 National Research Laboratories, Canada, "Effect of Flare on the Dynamic and Static Moment Characteristics of a Hemisphere - Cylinder Oscillating in Pitch at Mach Numbers from 0.3 to 2.0," by J. G. LaBerge, NCC LR-295, January 1961 (U)

- B. 87 AEDC, "Static and Dynamic Stability Tests of a 0.70-Scale Model of the Polaris Re-Entry Configuration at Transonic Speeds," by T. M. Perkins and C. D. Riddle, AEDC-TN-60-220, January 1961 (C)
- B. 88 -----, "An Investigation of the Influence of Several Shape Parameters on the Dynamic Stability of Ballistic Re-Entry Configurations," by J. A. Black, AEDC-TR-60-15, March 1961 (C)
- B. 89 AGARD, "Static and Dynamic Stability of Blunt Bodies," by H. C. DuBose, AGARD 347, April 1961 (U)
- B. 90 R. A. Kilgore and B. T. Averett, "A Forced Oscillation Method for Dynamic Stability Testing," Journal of Aircraft, Vol. 1, No. 5, pp 304, 305, Sept. - Oct. , 1964

Lockheed internal data were used extensively in the analysis, much of which is not published or intended for publication. The following reports are, however, available.

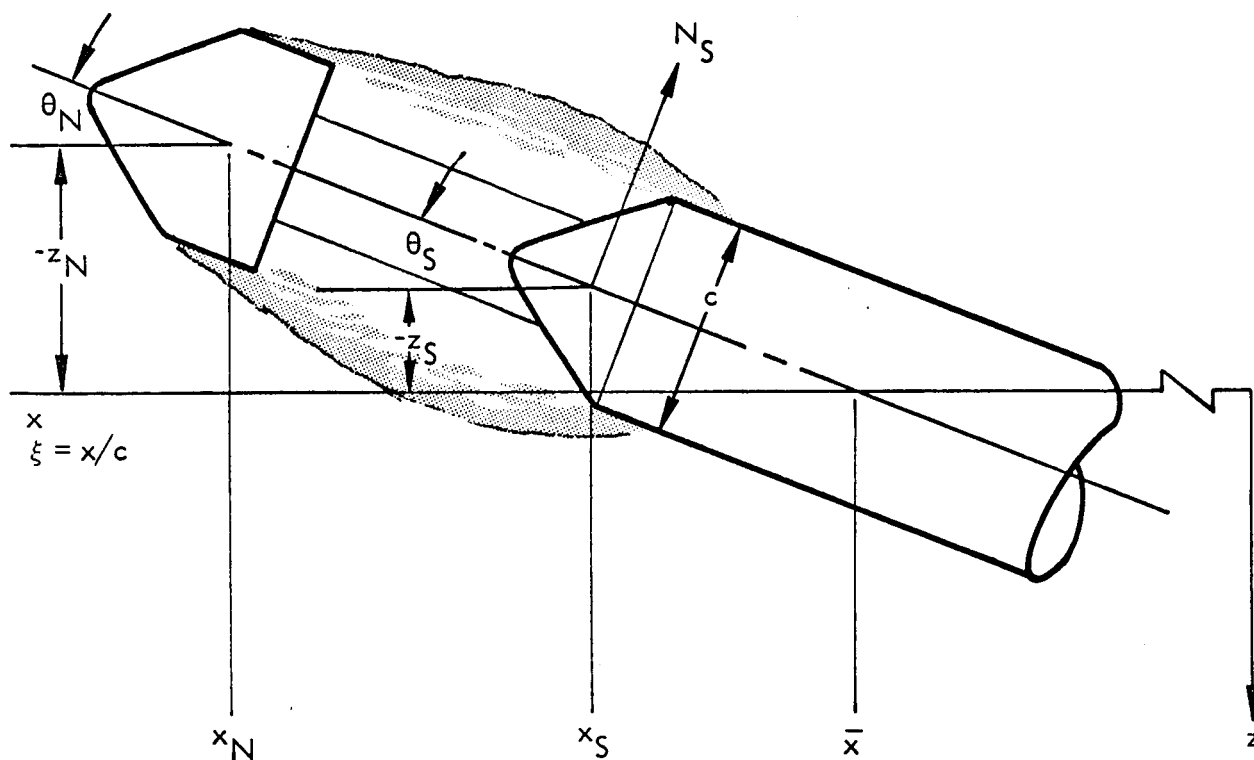
- B. 91 Lockheed Missiles & Space Company, "Relation Between Static and Dynamic Characteristics for a Slowly Oscillating Blunt Re-Entry Body With Non-Linear Amplitude Effects, Part I, Pitch Oscillations About a Fixed Axis," by L. E. Ericsson, LMSC TM-53-40-100, Dec 1959 (C)
- B. 92 -----, "Preliminary Data Release for the Transonic Wind Tunnel Tests of the Saturn-Apollo 5% Model," by J. P. Reding, LMSC TM 53-40-122 (LMSC/802367), Nov 1962 (U)
- B. 93 -----, "Preliminary Data Release for the Supersonic Wind Tunnel Tests of the Saturn-Apollo 5% Model," by J. P. Reding, LMSC TM 53-40-123 (LMSC/802593), Dec 1962 (U)

Appendix C

GENERALIZED QUASI-STEADY METHODS

The quasi-steady methodology was thoroughly discussed in Ref. 4. The present Appendix is intended to generalize and simplify the mathematical definition of the quasi-steady forces in regions of separated flow. Some repetition of the material presented in Ref. 4 is unavoidable in order to make the appendix comprehensible.

The normal force N_s on a body element submerged in separated flow can be expressed in the following way using the definitions in Sketch C-1. (A similar expression is obtained for the axial force moment (M_{A_s}) .



Sketch C-1

C-1

$$N_s = \frac{\rho U^2}{2} S \left\{ \frac{\partial C_{N_s}}{\partial \alpha_N} \alpha_N + \frac{\partial C_{N_s}}{\partial z} \Delta z + \frac{\partial C_{N_s}}{\partial \alpha_s} \alpha_s \right\}^* \quad (C-1)$$

where

$$\alpha = \theta + \frac{\dot{z}}{U} ; \Delta z = -(z_N - z_s)$$

and

$$\begin{aligned} \rho U^2/2 &= \text{dynamic pressure} \\ S &= \text{reference area} \end{aligned}$$

In the nonstationary case, the quasi-steady values of α_N and Δz are the value at a time Δt earlier than the local instantaneous value for α_s . That is,

$$N_s(t) = \frac{\rho U^2}{2} S \left\{ \frac{\partial C_{N_s}}{\partial \alpha_s} \alpha_s(t) + \frac{\partial C_{N_s}}{\partial \alpha_N} \alpha_N(t - \Delta t) - \frac{\partial C_{N_s}}{\partial z} [z_N(t - \Delta t) - z_s(t)] \right\} \quad (C-2)$$

Δt is the time required for the force N_s to respond to changes in α_N and z_N .

One may also express Eq. (C-2) in the following form:

$$\left. \begin{aligned} N_s(t) &= \frac{\rho U^2}{2} S \left\{ \widetilde{C_{N_s}}(t) + \Delta^i \widetilde{C_{N_s}}(t) \right\} \\ \widetilde{C_{N_s}}(t) &= \frac{\partial C_{N_s}}{\partial \alpha_s} \alpha_s(t) \\ \Delta^i \widetilde{C_{N_s}}(t) &= \frac{\partial C_{N_s}}{\partial \alpha_N} \alpha_N(t - \Delta t) - \frac{\partial C_{N_s}}{\partial z} [z_N(t - \Delta t) - z_s(t)] \end{aligned} \right\} \quad (C-3)$$

*The expression for M_{A_s} is (c = reference length)

$$M_{A_s} = \frac{\rho U^2}{2} S c \left\{ \frac{\partial C_{m_{A_s}}}{\partial \alpha_N} \alpha_N + \frac{\partial C_{m_{A_s}}}{\partial z} \Delta z + \frac{\partial C_{m_{A_s}}}{\partial \alpha_s} \alpha_s \right\}$$

where

$$\alpha_s(t) = \theta_s(t) + \frac{\dot{z}_s(t)}{U}$$

$$\alpha_N(t - \Delta t) = \theta_N(t - \Delta t) + \frac{\dot{z}_N(t - \Delta t)}{U}$$

The separation-induced force $\widetilde{\Delta^i C_N}(t)$ can be written

$$\widetilde{\Delta^i C_N}(t) = \Delta^i C_{N_\alpha} \cdot \alpha_N(t - \Delta t) + \Delta^i C_{N_\beta} \cdot \beta(t - \Delta t) \quad (C. 4)$$

where

$$\Delta^i C_{N_\alpha} = \frac{\partial C_{N_s}}{\partial \alpha_N}$$

$$\Delta^i C_{N_\beta} = L \frac{\partial C_{N_s}}{\partial z}$$

$$\beta(t - \Delta t) = - [z_N(t - \Delta t) - z_s(t)] / L$$

$$L = x_N - x_s$$

$$\alpha_N(t - \Delta t) = \theta_N(t - \Delta t) + \frac{\dot{z}_N(t - \Delta t)}{U}$$

For single degree of freedom pitching oscillations around x_{CG} the following holds

$$\left. \begin{aligned} \theta_N &= \theta_s = \theta \\ z_N &= - (x_N - x_{CG}) \theta \\ z_s &= - (x_s - x_{CG}) \theta \end{aligned} \right\} \quad (C. 5)$$

Eqs. (C. 3), (C. 4), and (C. 5) give

$$\left. \begin{aligned}
 \widetilde{C_N(t)} &= C_{N_{\alpha_s}} \cdot \alpha_s(t) \\
 \Delta^i \widetilde{C_N(t)} &= \Delta^i C_{N_{\alpha}} \alpha_N(t - \Delta t) + \Delta^i C_{N_{\beta}} \beta(t - \Delta t) \\
 \alpha_s(t) &= \theta(t) - \frac{(x_s - x_{CG}) \dot{\theta}(t)}{U} \\
 \alpha_N(t - \Delta t) &= \theta(t - \Delta t) - \frac{(x_N - x_{CG}) \dot{\theta}(t - \Delta t)}{U} \\
 \beta(t - \Delta t) &= \frac{x_N - x_{CG}}{x_N - x_s} \theta(t - \Delta t) - \frac{x_s - x_{CG}}{x_N - x_s} \theta(t)
 \end{aligned} \right\} \quad (C. 6)$$

For slow oscillations, when

$$\left(\frac{(x_N - x_{CG}) \dot{\theta}}{U} \right)^2 \ll 1 \quad \text{and} \quad \left(\frac{(x_s - x_{CG}) \dot{\theta}}{U} \right)^2 \ll 1$$

the angles $\alpha_s(t)$, $\alpha_N(t - \Delta t)$ and $\beta(t - \Delta t)$ can be expressed as follows:

$$\left. \begin{aligned}
 \alpha_s(t) &= \theta \left(t - \frac{x_s - x_{CG}}{U} \right) \\
 \alpha_N(t - \Delta t) &= \theta \left(t - \Delta t - \frac{x_N - x_{CG}}{U} \right) \\
 \beta(t - \Delta t) &= \frac{x_N - x_{CG}}{x_N - x_s} \left[\theta(t - \Delta t) - \frac{x_s - x_{CG}}{x_N - x_{CG}} \theta(t) \right]
 \end{aligned} \right\} \quad (C. 7)$$

That is, Eq. (C.6) may be expressed

$$\left. \begin{aligned} \widetilde{C_N(t)} &= C_{N_{\alpha_s}} \theta(t - \widetilde{\Delta t_s}) \\ \Delta^i C_N(t) &= \Delta^i C_{N_{\alpha}} \theta(t - \Delta t - \widetilde{\Delta t_N}) + \Delta^i C_{N_{\beta}} \frac{x_N - x_{CG}}{x_N - x_s} \left[\theta(t - \Delta t) - \frac{x_s - x_{CG}}{x_N - x_{CG}} \theta(t) \right] \end{aligned} \right\} \quad (C.8)$$

where

$$\begin{aligned} \widetilde{\Delta t_s} &= (x_s - x_{CG})/U \\ \widetilde{\Delta t_N} &= (x_N - x_{CG})/U \\ \Delta t &= (x_N - x_s)/\bar{U} \\ \bar{U} &\leq U \end{aligned}$$

That is, all the force components that produce dynamic effects have the following general expression

$$C_F(t) = C_{F_{\alpha}} \theta(t - \Delta t - \widetilde{\Delta t}) \quad (C.9)$$

For the elastic body, Eq. (C.5) becomes

$$\left. \begin{aligned} \theta_N &= \varphi'(x_N) \cdot q(t) \\ \theta_s &= \varphi'(x_s) \cdot q(t) \\ z_N &= -\varphi(x_N) \cdot q(t) \\ z_s &= -\varphi(x_s) \cdot q(t) \end{aligned} \right\} \quad (C.10)$$

This gives the following expressions for α_s , α_N and β in Eq. (C.6)

$$\left. \begin{aligned} \alpha_s(t) &= \varphi'(x_s)q(t) - \frac{\varphi(x_s)\dot{q}(t)}{U} \\ \alpha_N(t - \Delta t) &= \varphi'(x_N)q(t - \Delta t) - \frac{\varphi(x_N)\dot{q}(t - \Delta t)}{U} \\ \beta(t - \Delta t) &= [\varphi(x_N)q(t - \Delta t) - \varphi(x_s)q(t)]/(x_N - x_s) \end{aligned} \right\} \quad (C.11)$$

Thus, for slow oscillations the equation corresponding to Eq. (C.7) is

$$\left. \begin{aligned} \alpha_s(t) &= \varphi'(x_s)q\left(t - \frac{\varphi(x_s)/\varphi'(x_s)}{U}\right) \\ \alpha_N(t - \Delta t) &= \varphi'(x_N)q\left(t - \Delta t - \frac{\varphi(x_N)/\varphi'(x_N)}{U}\right) \\ \beta(t - \Delta t) &= \frac{\varphi(x_N)}{x_N - x_s}q(t - \Delta t) - \frac{\varphi(x_s)}{x_N - x_s}q(t) \end{aligned} \right\} \quad (C.12)$$

That is, Eq. (C.8) corresponds for the elastic body to the following equation

$$\left. \begin{aligned} \widetilde{C_N(t)} &= C_N \varphi'(x_s)q(t - \widetilde{\Delta t_s}) \\ \Delta^i C_N(t) &= \Delta^i C_N \varphi'(x_N)q(t - \Delta t - \widetilde{\Delta t_N}) \\ &\quad + \Delta^i C_N \frac{\varphi(x_N)}{x_N - x_s} \left[q(t - \Delta t) - \frac{\varphi(x_s)}{\varphi(x_N)} q(t) \right] \end{aligned} \right\} \quad (C.13)$$

where

$$\begin{aligned} \widetilde{\Delta t_s} &= [\varphi(x_s)/\varphi'(x_s)]/U \\ \widetilde{\Delta t_N} &= [\varphi(x_N)/\varphi'(x_N)]/U \\ \Delta t &= (x_N - x_s)/\bar{U} \end{aligned}$$

That is, Eq. (C.9) is still valid if it is modified slightly

$$C_F(t) = C_{F_\alpha} \tilde{\theta}(t - \Delta t - \tilde{\Delta t}) \quad (C.14)$$

where, in the elastic case

$$\tilde{\theta}(t) = \varphi'(x)q(t)$$

$$\varphi'(x) = \begin{cases} \varphi'(x_s) \\ \varphi'(x_N) \\ \frac{\varphi(x_N) - \varphi(x_s)}{x_N - x_s} \end{cases} \quad \text{for} \quad C_{F_\alpha} = \begin{cases} C_{N_{\alpha s}} \\ \Delta^i C_{N_\alpha} \\ \Delta^i C_{N_\beta} \end{cases}$$

When the body curvature is negligible one can write

$$\varphi(x_s) = \varphi'(x_s)(x_s - x_{\text{node}})$$

$$\varphi(x_N) = \varphi'(x_N)(x_N - x_{\text{node}})$$

$$\varphi'(x_s) = \varphi'(x_N) = \varphi'(0)$$

$$\tilde{\theta}(t) = \varphi'(0) \cdot q(t)$$

Thus, Eq. (C.13) becomes identical with Eq. (C.8) with x_{CG} substituted with x_{node} .

Examining Eq. (C.8) further, one observes that Δt is always positive and represents a true time lag for all x_{CG} . However, $\tilde{\Delta t}$ is not always positive. When x_{CG} is larger than x_s and x_N , $\tilde{\Delta t}_s$ and $\tilde{\Delta t}_N$ become negative and represent phase leads rather than lags. For the elastic body x_{node} corresponds to x_{CG} and a movement of the nodal point produces the same effect as the CG movement for the rigid body.